National Library of Canada
Acquisitions and Bibliographic Services Branch
395 Wellington Street
Ottawa, Ontario
K1A 0N4

Bibliothèque nationale du Canada
Direction des acquisitions et des services bibliographiques
395, rue Wellington
Ottawa (Ontario)
K1A 0N4

Your file Votre référence

Our file Notre référence

NOTICE

The quality of this microform is heavily dependent upon the quality of the original thesis submitted for microfilming. Every effort has been made to ensure the highest quality of reproduction possible.

If pages are missing, contact the university which granted the degree.

Some pages may have indistinct print especially if the original pages were typed with a poor typewriter ribbon or if the university sent us an inferior photocopy.

Reproduction in full or in part of this microform is governed by the Canadian Copyright Act, R.S.C. 1970, c. C-30, and subsequent amendments.

AVIS

La qualité de cette microforme dépend grandement de la qualité de la thèse soumise au microfilmage. Nous avons tout fait pour assurer une qualité supérieure de reproduction.

S'il manque des pages, veuillez communiquer avec l'université qui a conféré le grade.

La qualité d'impression de certaines pages peut laisser à désirer, surtout si les pages originales ont été dactylographiées à l'aide d'un ruban usé ou si l'université nous a fait parvenir une photocopie de qualité inférieure.

La reproduction, même partielle, de cette microforme est soumise à la Loi canadienne sur le droit d'auteur, SRC 1970, c. C-30, et ses amendements subséquents.

Canada

YIELDS OF MULTICHARGED IONS SCATTERED AND RECOILED FROM A CLEAN SILICON SURFACE

By

Pierre Gauthier

A thesis submitted to
the School of Graduate Studies and Research
in partial fulfillment of the requirements
for the degree of Ph.D. in Physics

Department of Physics

University of Ottawa
Ottawa, Ontario
10/12/93

ISBN 0-315-95920-7

Canada

Abstract

This thesis investigates the basic interactions of energetic ions with the top atoms on a clean surface. This information is of relevance to impact collision ion scattering spectroscopy (ICISS) investigations of surface structure. Using a variety of ions with energies in the keV range e.g. C^+, N^+, O^+, F^+, Ne^+, P^+, S^+, Cl^+ and Ar^+, incident upon a clean amorphous silicon surface, the outgoing particles were found to contain a significant fraction of multiply charged ions. Note that the ejected ions were energy analysed with a cylindrical electrode electrostatic analyser, designed and built by us, which had a sufficiently large solid angle of acceptance so that good energy spectra could be obtained with beam fluxes which did not significantly damage the surface structure. To explain the appearance of these multicharged ions, a charge exchange model is described that considers the interaction domain to be divided into three steps: the incoming trajectory, the close encounter and the outgoing trajectory. A definite threshold distance of closest approach for the production of each of the multicharged ion species was found. These threshold distances directly confirm the model in which multiply charged ions are created in binary encounters by molecular orbital electron promotion, and then are partially neutralized as they leave the surface. The molecular orbital correlation diagram can associate particuliar crossings responsible for each multicharged ion species observed.

Acknowledgements

I would like to express my sincere thanks to Dr. Brian Hird for the confidence and patience he showed and the time he spent with me throughout the past four years. I would like to thank Dr. Robert A. Armstrong for all his help and meaningful insight into our field of research. Many thanks to Bob Hart, Ron, Herve, Len and Francois, for all the excellent machining, shop work and loan of their tools. Thanks also to Mike Murphy in the electronic shop for is constructive advice and help. Finally, I would like to express my deep appreciation to my wife and parents, whose backing and support made this thesis possible.

Contents

List of Tables

List of Figures

Chapter 1. Introduction

The scattering of ions from surfaces is a well established field of physics. In many cases it is studied to elucidate the structure of the surface involved. The application of low-energy ion scattering (LEIS) techniques to the study of the composition and structural arrangement of solid surfaces has developed considerably in the past few years[2]. The aim of these experiments was to obtain information about the scattering process itself, channeling and blocking effects and neutralisation processes. These interactions have been found to depend on the geometry of the atoms in the first few surface layers so that ion scattering is one of the techniques available to obtain structural information about surfaces. It complements the information from electron scattering in which a Fourier transform from momentum space is required whereas ion scattering data is analysed in real geometric space.

For certain ranges of ion energies and scattering geometry, surface species can generally be identified by the presence of surface scattering peaks in the scattered ion energy spectrum and the surface concentration of these species can be related to the size of these peaks. The energies of scattered and recoiled particles can be predicted very accurately by using classical physics and describing the process as binary collisions involving a central force e.g. the binary collision model. Such a simple model is adequate for identifying spectral peaks; the analysis of multiple collision trajectories and inelastic energy losses require more rigorous models.

A basic problem in low energy ion-surface scattering, since the early work of Hagstrum[3], has been the mechanism of charge transfer (see the review by Boers[4]). As low energy ions are used in many aspects of surface analysis, it is essential that the processes which are responsible for the loss of ions through neutralisation in these techniques be understood. Because several charge changes may occur in sequence, the interpretation is complicated. It is therefore useful, at least conceptually, to separate the surface encounter into three steps - a) the ingoing region from the

initial encounter with the surface average potential through the increasing influence of separate atoms to a region b) where a close encounter with an individual atom significantly changes the direction of the trajectory, and then c) a final or outgoing region where there are more gentle interactions. For certain projectile-target combinations, there is strong evidence that the final charge state is independent of the incoming ion beam charge, and that the ingoing interactions do not significantly affect the outgoing charge state fractions[5, 7]. The attractiveness of the "loss of memory" assumption is that it simplifies the interpretation of charge state fractions. The only surface structure dependent interactions which affect the charge fractions are then in the outgoing part of the trajectory. The theory predicts very well the observed dependence of the charge fraction on the energy states of the electron in the ion and in the surface[8]. Extensive experimental and theoretical work has been done on the scattered charge fractions when singly charged ions or neutrals are scattered from clean surfaces but very little work on multicharged ions. A few investigations at high energies were made in the late 1960's but since then, there have been no further investigations until the present systematic survey. Meanwhile, the field of Auger electron spectroscopy (AES) has evolved considerably. Interpretations of these electron yields has conventionally relied on assumptions about the decay of multicharged ions which are seriously put into question by the present investigations.

Using a slightly modified $\pi/\sqrt{2}$ electrostatic analyser (ESA), we performed the first low-energy investigation of multicharged ion creation resulting from well defined ion surface collisions. These multicharged ions simplify the analysis since they can only be created in the close encounter region of the interaction by inner shell electron promotion so that the initial beam charge and any changes in the charge during the ingoing trajectory are unimportant.

The most widely used technique for surface structure analysis is the time-of-flight (TOF) technique. As usually employed, this technique cannot separate out multicharged ions from singly charged ions. The reason for this drawback lies not in the basic way in which this technique works but in the designs used. The TOF technique consists in a pulsed ion beam of a few keV which strikes a target surface, and

the velocity spectrum of the scattered and recoil particles is obtained by measuring their flight times from the sample to the detector. This technique collects emitted ions and neutrals of all energies at the same time with the option of removing with an electrostatic clearing field all ions (e.g. singly and multiply charged ions) from the particle flux which reaches the detector.

Chapter 2. Useful aspects of ion scattering theory

2.1 The binary collision model

When an energetic ion is scattered by a single atom its energy after the collision depends on the kinetics of the elastic collision and on the inelastic energy losses. For primary energies in the keV range, the elastic energy loss is far greater than the inelastic energy losses which will be ignored in this work. Ion-surface scattering at a few hundred eV to a few keV energy has been extensively used for surface characterization under circumstances where most of the detected ions have undergone a single elastic collision with an atom at the surface. The use of this simple collision model is justified because the interaction time of the collisions is short compared to the period of phonons of the solid targets. Due to the small de Broglie wavelength of the ion, we can treat the interaction classically and can neglect quantum-mechanical effects. In other words, for ion energies in the keV range, the binary elastic collision model provides a good first order description of ion-surface collision kinematics and the laws of conservation of energy and momentum can be used to describe scattered trajectories and energies. Second order effects due to neighboring atoms and solid state properties modify these predictions. For example, differences are found between ion-gas and ion-solid scattering involving the same ion-atom elements.

Although a complete classical dynamics calculation which takes into account individual trajectories is required for spectral simulation, the major spectral features of scattered particles can be classified into two simple categories; quasi-single scattering (SS) and quasi-multiple scattering (MS). The prefix "quasi" is used to emphasize that the description is greatly oversimplified, i.e. both the scattering and recoiling trajectories are influenced by more than just one collision partner. However, for the purpose of spectral interpretation, it is extremely useful to have such simple classifications for the major features. SS represents the case of one large

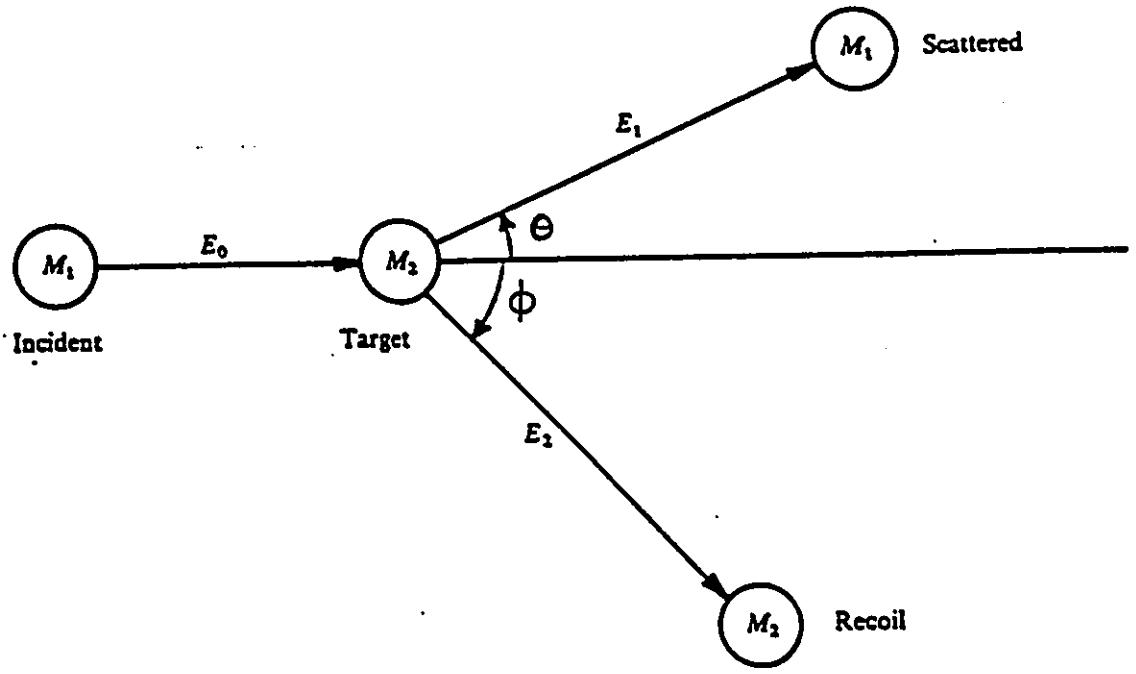

Figure 2.1: Kinematic diagram of the scattering geometry

angle deflection that is preceded and followed by a few very small deflections. A collision of the type seen in Fig.2.1 typically produces a sharp scattering peak whose energy is near that of the theoretical single collision energy.

The energy E_s of a particle scattered from a single collision is given by the following equation:

$$E_s = E_o \left[\frac{\cos\theta \pm (A^2 - \sin^2\theta)^{1/2}}{(1 + A)} \right]^2, \tag{2.1}$$

where

$$A = M_2 / M_1.$$

This equation is known as the kinematic equation for scattered particles and it is derived from conservation of momentum and energy. If the mass of the incoming particle is smaller than or equal to the mass of the target atom, $M_1 \leq M_2$ and

$A \geq 1$, then the positive sign in eq.2.1 is used. If $M_1 \geq M_2$ and $A < 1$, both signs give real physical solutions and the energy of the scattered particle is then found to be a double valued function of the scattering angle, i.e. there are two E_s for each θ. For this latter case, the maximum SS scattering angle is $\theta_{max} = sin^{-1}(A)$.

The observed scattered peaks in the energy spectra of experimental surface scattering measurements are found to agree closely with the predictions of this simple two body process. Atoms emitted from the surface can also be detected in the form of direct recoils when the surface is bombarded with energetic ions and again the kinetic energy can be calculated from classical laws. The energy E_r of a target atom of mass M_2 recoiling at an angle ϕ to the primary ion beam of energy E_o and mass M_1 is given by the kinematic equation for recoil particles.

$$E_r = E_o \left[\frac{4\,A\,(cos\,\phi)^2}{(1+A)^2} \right] \tag{2.2}$$

Both kinematic equations are plotted in Fig.2.2. In the scattering of an ion from a single crystal, polycrystalline or amorphous target, the influence of multiple interactions on the energy of the ion has to be taken into account in the description of the process. In general, MS represents the case of at least two large angle deflections in each ion surface interaction. This process can be described reasonably well by a series of successive binary collisions and the energy of the multiply scattered ion will be higher than the energy of an ion scattered through the same total angle by a single atom. The presence of substantial multiple scattering produces a scattering peak which is broader and at higher energy than the SS peak. The high-energy limit occurs for n collisions, each with scattering angle (θ/n), and this is calculated by repeated application of the kinematic equations for each large angle deflection. For example a forward angle scattering (40°) of oxygen on Si gives a single scattering energy of $E_s = 0.75E_o$ which is increased by 14% for two 20° scatterings. Unequal angle scatterings give lesser increases with the smallest increase occurring when one scattering angle is much larger than the others.

Besides the higher energy peak, MS sequences also produce a broad, low-intensity structure that lies beneath and extends to lower energies than the SS peak. This

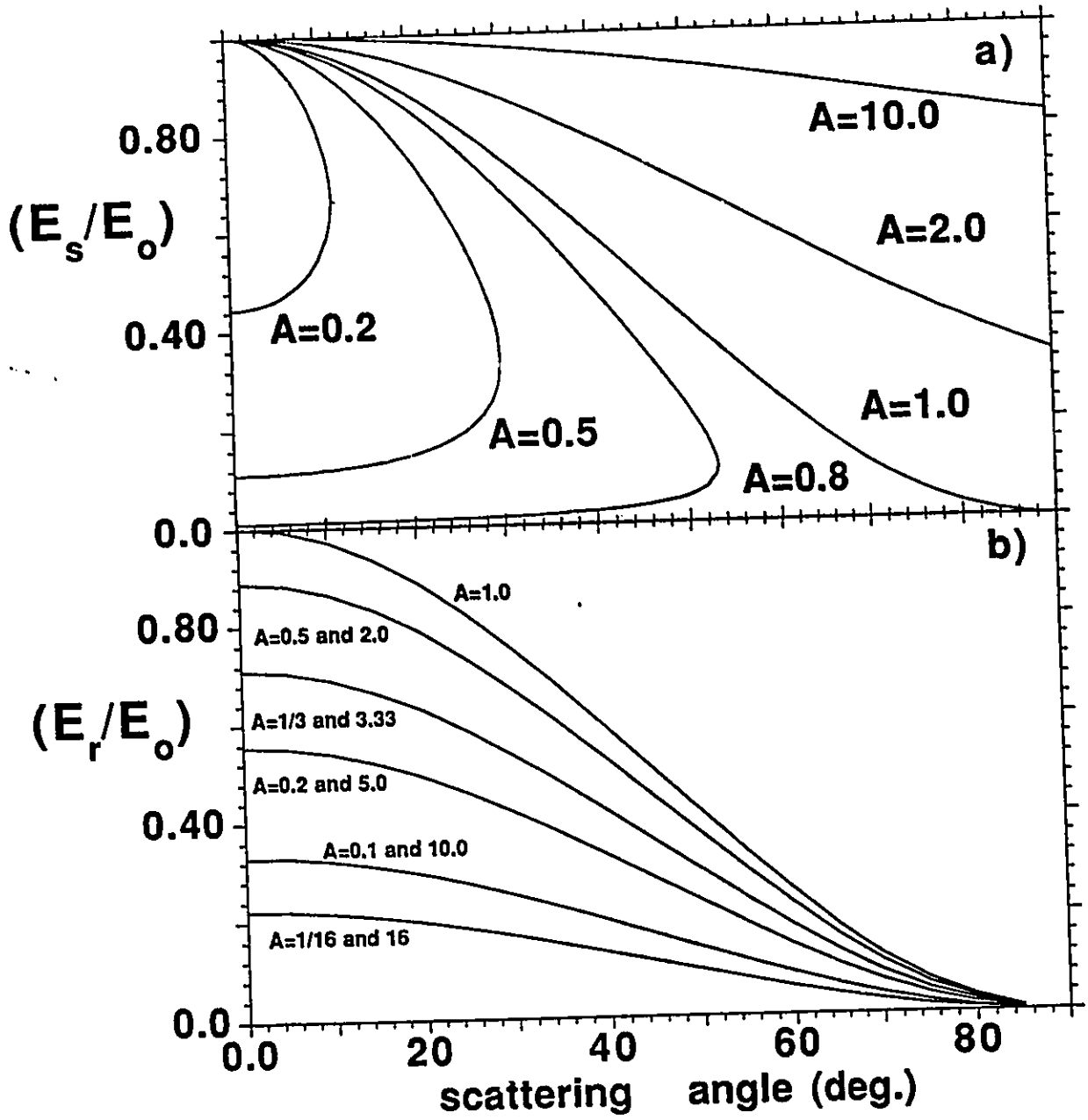

Figure 2.2: Kinematic curves for a) scattered and b) recoil atoms

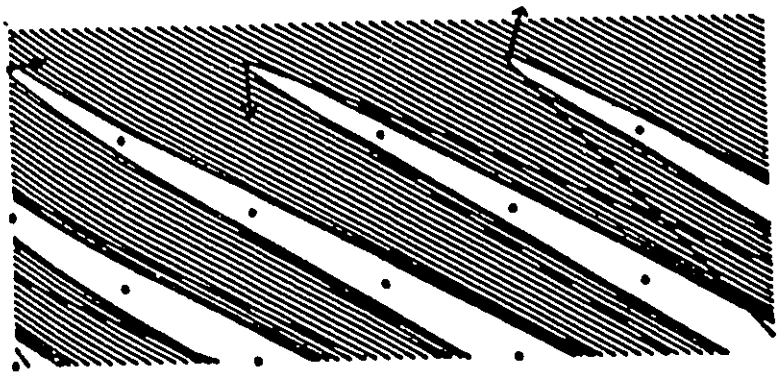

Figure 2.3: Shadow cone envelope

broad structure is a result of MS sequences in which a projectile penetrates below the outermost surface layer, loses energy in collisions and then re-emerges from the surface.

When an ion approaches an atom, the angle at which it scatters depends on the impact parameter of the trajectory. Small impact parameters result in backward scattering and large impact parameters result in forward scattering. The curvature of the path decreases with increasing impact parameter. The result is a region behind the target atom into which no ions can penetrate, this is described as the "shadow cone" because of its approximate shape.

The shadow cone (see Fig 2.3) can be obtained by calculating the trajectories for many different impact parameters and determining the envelope of the innermost trajectories since different trajectories touch the envelope in different regions of the shadow edge. The actual shape of the shadow cone depends on the interatomic potential used, the energy of the projectile and the masses of the colliding particles. Several parametrizations of the screened Coulomb potential have recently been produced which fit more and more closely to experimental ion-atom scattering data. This was first done by Molière with a simple two parameter potential.

2.2 Multicharged ion creation from ion-surface collisions

2.2.1 Introduction

The study of charge exchange between projectile atoms and a clean surface is of fundamental interest, both from a theoretical and an experimental point of view. Inelastic processes in ion-surface collisions can result in the conversion of translational kinetic energy into electronic excitation and ionization of the atoms in the collision pair. This electronic excitation of the scattered or recoiled particles can result in such phenomena as the emission of electrons and photons from the projectile or target species, shifts in the scattering energy from the elastic scattering position or variation of the charge state of the outgoing species.

In the past, most studies of inelastic collisional processes have been carried out in the gas phase where the number of inelastic channels is limited. The study of ion-surface collisions is complicated by the multitude of inelastic channels possible. One of the major goals of research in this area is to determine which of these inelastic channels are operative in specific ion-surface collisions. Projectiles scattered in distinct single binary collisions (SS) with a surface atom offer a unique opportunity to study inelastic ion-surface collisions in that their trajectories and velocities are well defined. The study of these well defined cases of primary particles allows the channels by which the translational energy of the primary ion is converted to electronic excitation and ionization energy to be determined.

2.2.2 Charge changing processes

Evidence that ions may pick up and also lose electrons on scattering from a solid surface was seen in the energy spectra of scattered ions obtained in early work by Datz and Snoek[10]. As low energy ions are used in many aspects of surface analysis it is important that the processes which are responsible for the loss or creation of ions be understood. Due to the atom-surface interaction, electrons can be transferred from the ion to the target atom or vice versa. Low energy ion scattering (LEIS) provides a very controlled method of studying the neutralisation process in that the

projectile path and history are well known for ions scattered off the surface layer by a single collision.

Electronic transitions in which an ion near a surface atom could conceivably become involved are of the radiative, Auger and resonance tunneling types. However Schekter[11] has shown that the probability of neutralization of an ion near a metal accompanied by radiation is very low (about 5×10^{-7}). The probability of any radiative process is expected to be low because the lifetime for radiation (about 10^{-8} sec) is very long compared to the time which even a thermal particle spends within a few angstrom units of the surface (of the order of 10^{-15} sec considering an oxygen ion in the low-keV region).

The most commonly quoted theoretical treatment of these neutralisation processes is that of Hagstrum[3] who analysed the Auger process for ions with an energy of a few eV, using a time independent treatment. The transition rate was defined for a stationary ion as a function of distance from the surface. The integrated sum of that rate over the path of the ion then represented the probability of neutralisation. This approach results in the probability of an ion escaping the influence of the surface in a charged state being given by

$$P^+ = exp(-v_c / v) \tag{2.3}$$

where v is the perpendicular component of velocity of the ion and v_c is the characteristic velocity for the interaction which is made up of a transition rate A, and a screening length a. The value of v_c is a function of the electronic properties of the projectile and the solid, and within this model is expected to be constant at all energies.

Even though the Hagstrum approach is only suitable for slow moving ions (1 - 10 eV) it has been extensively used for low energy ions (0.1 - 10 keV) in circumstances where many of the assumptions involved in the model are not satisfied. The general form of behaviour for P^+ has been observed with low energy ions, but the energy independence of v_c has been shown to be invalid[12].

Bloss and Hone[13] showed that using the more rigorous Anderson-Newns time-dependent formalism to describe the charge exchange processes, the essential features of eq.2.3 were preserved for low energy ions. Further support for the validity of eq.2.3 as being appropriate for LEIS was supplied by Muda and Hanawa[14] who used the same time-dependent approach. In their study, the role of the band structure was examined in detail. A weak oscillation about the principal trend represented by the equation for P^+ was identified and associated with the finite width of the conduction band of the target.

While accepting that all possible charge exchange processes can operate simultaneously, the dominant process for the incident ion energies used in this work is resonance tunneling. It is therefore appropriate that we examine this process in greater detail. Resonant electron exchange is a pure one-electron process, which involves the transition of a single electron to or from the atom. In this model we consider only the conduction band of the target material and one energy level of the projectile atom. Deeper levels are tightly bound and cannot be excited because the motion of the atom and therefore the time-dependent perturbations acting on the electrons are too slow. For the same reason, no electrons can be excited into higher states, in particuliar into the electronic continuum above the vacuum level. Note that two-electron processes, such as the Auger process are much less probable than resonant tunnelling in cases where the latter is possible.

The general approach in describing the resonance process is based on a solution of the Anderson-Newns Hamiltonian. For simplicity, it is assumed that this process takes place in a single nondegenerate atomic state which lies energetically within the target atom conduction band, and for this atom, a free-electron description is assumed to be valid. Also the projectile atom's kinetic energy is assumed to be in the intermediate range (keV) and the atom-surface interaction is treated in a first-order rearrangement approach, as was proposed by Gadzuk[15] for the description of the chemisorption of alkali atoms on a metal surface. The unfilled electron states of the target atom are described by free waves inside a potential box with a total energy equal to the sum of the work function (ϕ_e) and the Fermi energy (E_F). Note that outside the box, the wave functions decay exponentially.

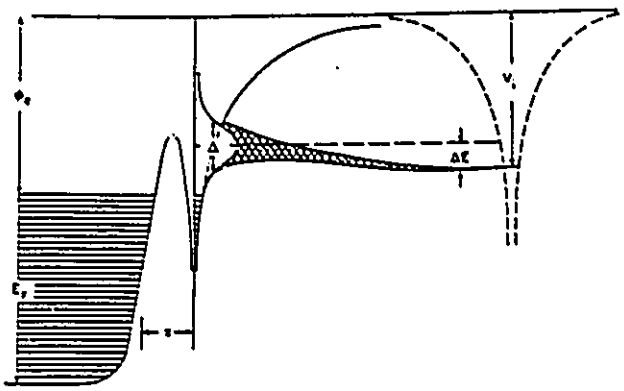

Figure 2.4: Energy level diagram of resonant charge transfer

When the projectile ion is brought close to the surface atom its originally sharp level shifts and broadens into a band of finite width due to interactions with electron bands in the solid. This interaction which is illustrated in Fig.2.4 can be composed of at least three components; van der Waals attractions, overlap of electronic wave functions and a Coulombic image force of attraction. Hagstrum[3] has shown that the polarizability of the ion is so small that the van der Waals forces are negligible for the range of ion energies of interest here. The overlap of electronic wave functions results in two effects; an attraction due to electron exchange resulting in the formation of covalent chemical bonds and a repulsion due to interpenetration of electron clouds and the Pauli exclusion principle. These effects are observed as the formation of molecular orbital (MO) combinations and MO promotion as the atomic orbitals of the colliding atoms overlap. Such effects will be discussed in more detail in the next section.

To first order the origin of the level shift (ΔE) can be understood with classical electrostatic theory. The Coulombic image force of attraction is due to the image potential induced in the metal surface electrons by the approaching ions. Compared to the situation at infinite atom-surface distance, the valence electron experiences

an extra repulsion from the image of the core and extra attraction of its own mirror charge. To first order the level shift is determined by the classical image potential where z is the atom-surface distance and k^{-1} takes into account the finite screening length of the target atom.

$$\Delta E = \frac{1}{4(z + k^{-1})}$$

The level width (Δ) is caused by the overlap of the incoming ion and target atom wave functions. This overlap makes resonant electron tunneling through the potential barrier between the ion and the atom possible. Simply stated, the probability for a resonant transition of the valence electron to an unoccupied target state determines the lifetime of the electron near the atomic core. This finite lifetime relates via Heisenberg's uncertainty relation to the level width. To first order, the level width is given by Fermi's golden rule where the sum has to be taken over all metal states $| k>$ degenerate with the atomic valence states $| a>$ at the energy ϵ_a.

$$\Delta(z) = 2\pi \sum \rho(\epsilon_a) |<a | V | k>|^2$$

The symbol ρ denotes the density of the metal states, which varies within the free-electron model as $\epsilon_k^{1/2}$. V is the unperturbed interaction of the valence electron with the ion core. To a good approximation, the level width is an exponentially decaying function of the atom-surface distance z. This perturbation-theoretical description of the interaction between an ion and a surface atom is useful if the width Δ of the atomic state is small with respect to the width of the conduction band. In this case, perturbation theory provides a picture of a relatively localized atomic state, perturbed by the presence of the target atom.

Note that in all studies to date the relative importance of the various electronic parameters of the projectile and the solid have not been clearly delineated. These electronic parameters may include the ionisation potential of the projectile, its possibly excited states, the work function of the surface, the valence band width and the density of states at the surface.

2.2.3 Three step collision model and the memory loss assumption

Over the years singly ionized scattered ion fractions have been measured for several ion-surface combinations. The fraction of scattered or recoiled particles in an ionized state as a result of a specific scattering or direct recoiling event will be referred to as the "ion fraction" or "ion yield". For noble gas and active ions on metal surfaces, the positive scattered ion yield ranges from $0-70\%$ while for alkali ions it is typically $> 80\%$. Several calculation techniques have been developed which give generally good agreement with experimental measurements. In order to understand the phenomena that contribute to this wide range in scattered ion fractions, the collision sequence must be analysed at all points of the scattering trajectory.

While a complete description of the interaction between an ion and a surface would be expected to adequately describe all aspects of the charge exchange process, no such model currently exists. Such a description must be capable of treating both the processes which can occur when the ion is near the surface and those which occur when the distance of closest approach in the collision is sufficiently small that the interaction is of the form encountered when two atoms in isolation collide. The empirical approach to this potentially complex interaction is to treat it as three independent regimes. Thus the approach to and the departure from the surface are treated as processes in which the energy levels in the projectile interact with the distributed states of the solid, while in the collisional regime the charge exchange processes are best modelled by molecular overlap models.

The collision process is effectively divided into three parts: a) the initial interaction before the primary ion actually reaches the target atom, b) the hard (binary) collision and finally c) the outgoing interaction between the two particles. Experimentally only the initial and final charge state of the primary ion are measurable, the intermediate part is not directly accessible. Multiple collisions may be included by traversing the region b) more than once, but this additional complication can be minimised by selecting the SS peaks in the energy spectrum of the emitted ions.

Since the early work by Hagstrum[3], who examined in detail the initial neutralization processes, it has become generally accepted that the first two parts of the

interaction do not contribute in determining the final charge state. In many theories it has been generally assumed that the scattering properties are independent of the initial charge state, and some of the formulations support this assumption. More recent formulations of the theory[16] give very small order of magnitude estimates for the survival probability of the initial charge state through the first two parts of the collision. For example, the observed neutral atoms in the scattering of a sodium atom beam from a tungsten surface are interpreted theoretically as ionized atoms which have been re-neutralized on the way out[16] rather than processes where the initial neutral state survives.

In spite of these theoretical models on ion neutralization the experimental data does not distinguish directly between neutralization on the way in and neutralization on the way out. One of the best test of the memory loss assumption was made by Bronckers and de Wit[7] who compared the angular distributions of Ne^+ and O^- (from fragmented incident H_2O^+ ions) scattered from Cu(110). They found that both Ne^+ ions and O^- ions show strong shadowing and blocking cone effects from first layer atoms consistent with a close encounter which is independent of the ingoing charge state. They concluded that the final charge state is determined during the outgoing part of the trajectory and that the charge state of the ion immediately before the collision is unimportant. A complication in interpreting the Bronckers and de Wit data is the low yield of Ne^+ scattering compared to the negative ion yield of oxygen, a consequence of the large rare gas ionization potential.

More recently clearer and more direct evidence was presented by Hird *et al.*[5] who took measurements of oxygen-silicon surface scattering, under binary collision conditions, and found the same ratio of negative to positive scattered ions under identical scattering conditions for both an incident O^- ion beam and an incident O^+ ion beam. The only previously reported measurements which compare otherwise identical positive and negative ion beam surface scattering are those of van Wunnik, Geerlings, Granneman and Los[17] for hydrogen scattering from tungsten covered with a monolayer of cesium. They initially found some differences in the negative hydrogen fractions in proton scattering from this surface which they explained as incomplete memory loss for proton-cesium scattering and complete memory loss

for proton-tungsten scattering. In an attempt to confirm this postulate they then compared the negative ion yields using positive and negative hydrogen beams under conditions which optimised the proportion of ions scattered from the cesium monolayer. In contradiction to their postulate they found no difference, within the accuracy of their measurements, between the negative ion yields for the differently charged beams. On the other hand some exceptions to the memory loss assumption have been found; for example, at energies below 10 keV the ion fraction scattered from a Cu surface, with an incident neutral Ne beam was found to be quite different from the scattered ion fraction with a Ne^+ beam[19].

Although the loss of memory assumption is in doubt for neutral and singly charged ion fractions, the distinction between the three interaction regions is quite clear for processes that produce multicharged ion species. Multicharged ions can only be created in the close encounter part of the interaction by inner shell electron promotion under conditions which are sufficiently violent to erase the existing valence electron structure, which means that the initial projectile charge state and any charge exchange occurring in the ingoing trajectory are unimportant. Electronic transitions and electronic promotions can occur in the close atomic encounter where the atomic orbitals of the colliding atoms merge into molecular orbitals of a quasi-diatomic molecule. Such electron promotions can result in neutralization of the projectile or ionization of either the projectile or the recoil atom as well as production of multicharged ions of both atoms involved in the collision. Rigorous calculations of the electronic transition probabilities or charge exchange probabilities in the close encounter and along the incoming and outgoing trajectories have been done. Such calculations represented an active area of research about 15 - 20 years ago.

The processes occurring in the close encounter have strong dependence on the actual distance between the colliding atoms. The distance of closest approach (r_o) can be calculated from scattering calculations. Plots of r_o versus E are shown in Fig.2.5 along with the distances corresponding to the sum of the radii of maximum charge density for various combinations of electronic shells of importance in C^+ and Ne^+ collisions with Si. The plots show that for incidence energies greater than about

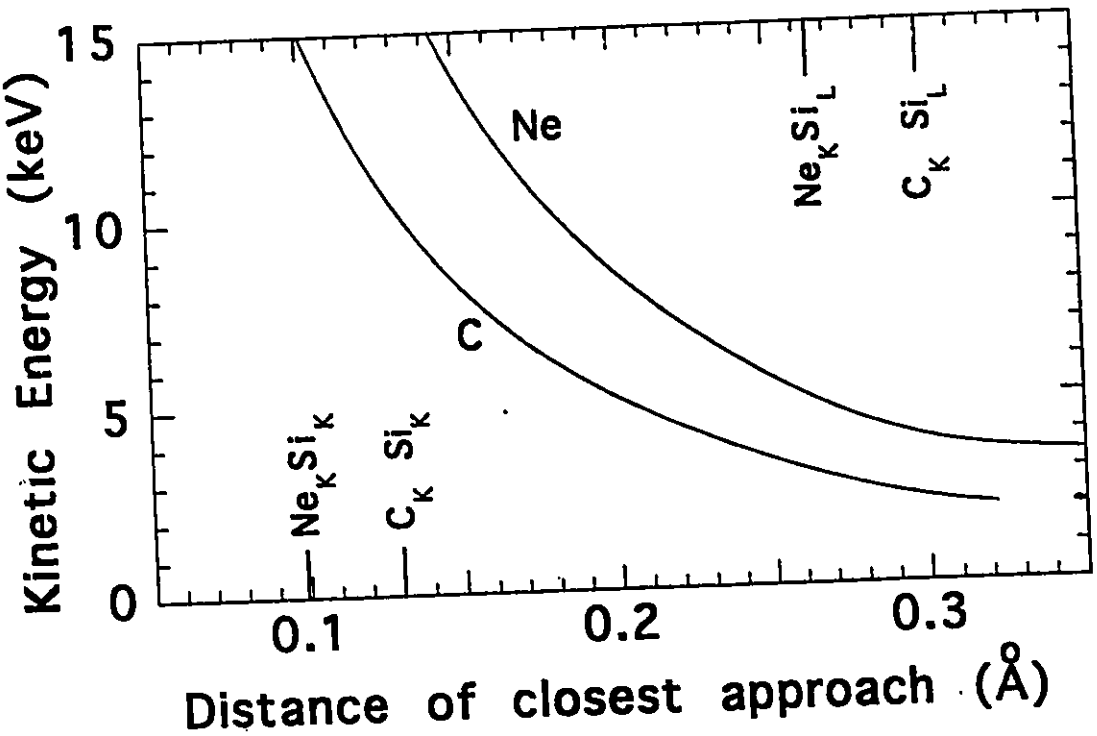

Figure 2.5: Calculated distances of closest approach versus primary ion kinetic energy for C-Si and Ne-Si collisions at 45°[6]. The sum of the radii of maximum radial charge density for various combinations of the L and K shells are indicated on the figure.

3 keV, significant penetration of the core atomic shells is achieved.

When experimental conditions are such that the velocities of inner-shell electrons are much larger than the relative speed of the colliding pair, specific electron promotion in the close encounter can be predicted by constructing separated-united atom diagrams and using the concept of diabatic molecular states. Diagrams such as Fig.2.6 show that as the separated atoms approach, a quasimolecule is formed. During small interaction distances (typically $< 1\mathring{A}$), electrons may be transferred between molecular orbitals (MO) which are nearly but not quite degenerate in the static MO calculations (diabatic crossings). The transfer occurs due to the non-static nature of the states. If an electron does not transfer back at the second traversal of the diabatic crossing, the final separated atom states differ from the

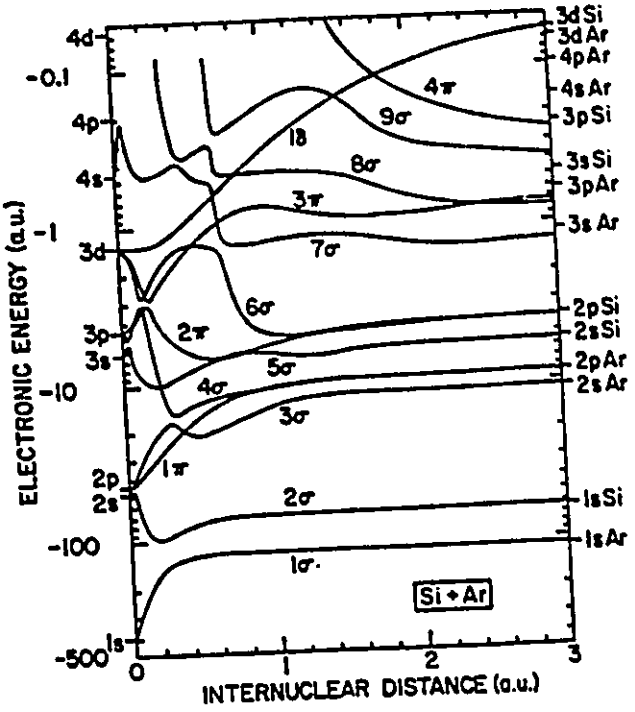

Figure 2.6: United-separated atom correlation diagram for electrons in the field of two differently charged nuclei.[taken from 58]

initial states, and as the atoms recede from each other, an electron then may end off with high excitation and an inner-shell vacancy is left in the initial orbit. The resulting electronic configurations yield highly excited discrete states whose lifetime (10^{-7} - 10^{-9} sec.) are longer than the collision times (10^{-13} - 10^{-15} sec.).

2.2.4 Other experiments which give information on final charge states

The first examination of multiply charged ion production under well defined scattering conditions was performed by Datz and Snoek[10] using 40-80 keV Ar^+ ions scattered from copper single crystal and polycrystalline surfaces. Van der Weg and Bierman[20] repeated these measurements in more detail. They compared their ion-solid (copper target) outgoing charge fractions with similar measurements using a Cu vapor target. They were able to fit the smaller multiply charged ion fractions

from the solid with calculations starting from the ion-vapor charge fractions and assuming that these decayed with a Hagstrum type exponentially decreasing interaction on the way out of the solid. Barth, Mühling and Eckstein[21] observed both recoil and scattered multiply charged fractions in Ar^+ and Ne^+–Ti and Ni surface scattering at 9 keV. They measured the energy and exit angle variation of the charge fractions, and found an exponential dependence on the perpendicular component of the exit velocity, again in agreement with a Hagstrum type interaction. Winter[22] identified N^{2+} and N^{3+} ion fractions when 350 keV N^+ incident ions were scattered through 0.8° from a polycrystalline copper surface.

Electron and x-ray spectra from ion-surface bombardement

There is much indirect evidence of multicharged ion production in ion-solid interactions from electron and X-ray emission measurements. The energies associated with atomic energy levels of both the projectile and the solid can be clearly identified[23]. These generally agree with the inner shell vacancy filling model developed from ion-gas collision data, with some differences in the states populated. The inner shell vacancy filling model was originally developed to explain ion-gas scattering data and X-ray emission data from solids.

A limitation of these measurements is that the ion trajectories which produce the observed electrons or x-rays are not well defined. Although Doppler effects establish that the ion is moving, these effects are too small to accurately deduce the ion direction at the moment of emission. The observed spectra are thus the integrated results from all ion trajectories.

Experiments that investigate Auger electrons which are emitted when a multicharged incident ion beam interacts with a solid[24] examine a quite different phenomenon. These observed Auger transitions occur during the ingoing part of the ion-solid interaction, whereas multicharged ions created during the close encounter, which are the main emphasis of our work, only undergo Auger transitions on the way out. Measurements of the electron spectra when a low energy multicharged incident ion beam interacts with a metal surface have been made by deZwart and

by Varga[25] and analysed in detail with a model which was successful in fitting the observed energy spectra by combining the predictions from Auger, Penning and resonance transitions. The fit provides estimates of the relative importance of these different interaction processes. The

review see Valeri[32]. A weak line in the Auger spectrum has been attributed to the decay from double vacancy excitations, and the incident ion energy threshold to produce this line was found to be considerably higher than for the other Auger transitions. Such double vacancies are probably necessary for the production of multicharged ions. However it is only in p-t collisions that both vacancies are likely to be produced in one partner since symmetric collisions strongly favor one vacancy in each partner. Asymmetric p-t collisions may thus be the main source of multicharged ions, even though symmetric t-t collisions are the main source of Auger electrons.

Deductions about the collision processes which create multicharged ions are very indirect from both SIMS and Auger electron measurements. SIMS measures low energy ions which have made many collisions before they are detected by the quadrupole mass spectrometer. Auger electrons are emitted approximately isotropically in the moving frame of the ion or atom which emits them, so that its direction is unknown apart from a small Doppler shift, so that only a statistical average is obtained.

In the measurements reported here the collision trajectories are well defined. We select peaks in the energy spectrum of the emitted ions which agree well with the energies predicted from single binary encounters, where either the incident ion or the recoil atom is scattered directly out of the surface without further loss of energy. Both correspond to the asymmetric p-t process. In contrast to the situation at higher energies[33], the average charge of the emitted ions from binary collisions is found to be less than in corresponding ion-gas collisions.

Chapter 3. Experimental Apparatus

3.1 Introduction

In order to do LEIS measurements, one must have a system similar to the one shown in Fig.3.1. The ions are extracted from the source, accelerated to a desired velocity, mass selected and then focussed through two slits, onto a point several meters away from the source. This narrow ion beam which has a well defined energy and angular spread strikes an atomically clean silicon surface located at the center of a 25 cm diameter ultra-high vacuum (UHV) chamber. The ejected particles are energy analyzed with an electrostatic analyzer (ESA) which has angular and energy resolution and which can be rotated around the target for angular distribution measurements. Although the rest of the apparatus was mostly constructed by copying standard techniques, the ESA represents an original design. All previous designs required much higher ion fluxes on the target and occupied much larger scattering chambers. Target cleanliness is obtained by sputtering the sample followed by annealing. Additionnally, the crystal structure can be determined using our reflection high energy electron diffraction (RHEED) system fitted as a diagnostic tool inside the UHV chamber where it did not interfere with the ESA.

3.2 Ion production

The ions we use are produced by a radio-frequency (RF) ion source. This type of ion source extracts positive ions from a plasma (in the keV range) in fluxes of the order of microamps (μA). Additionally it provides the option of creating both positive and negative ion beams. Other types of ion source are available which avoid the main restriction of the RF source which is that the source element must be in the gaseous form for most of the beams produced. However these are less reliable, or have short maintenance intervals or produce very low intensity beams. They almost always use

thermionically emitted electrons from a hot filament to ionise the atoms, so that negative ion extraction is not possible because of the large electron background.

The discharge is produced inside a glass tube by external electrodes coupled to a high frequency oscillator. The radio-frequency waves excite the gaseous atoms or molecules by creating a strong electro-magnetic disturbance. Sufficient RF power is required to fill most of the volume with plasma. A positive anode, in this case a wire, is sealed into the glass tube and since the plasma is basically a conductor, the whole of the discharge comes to an equilibrium within a few volts of the positive anode potential (typically 1 kV) because of the much higher mobility of the electrons compared to the positive ions.

The only other conducting surface exposed to the plasma discharge is an axial-tube electrode, usually called the exit canal. The ionized atoms are extracted from the positively biased plasma boundary and subsequently accelerated towards the canal where some escape into a much lower pressure region. Inside the tube the ions are in a nearly field-free region before emerging into the roughly uniform electric field of the accelerator column. The fringe field between these two regions behaves as an ion optics lens. It provides focussing so that the beam can be converged to a small width beyond the accelerator.

The energy of the ions is determined by the potential change between the plasma and ground and is approximated by the sum of the anode potential and the accelerator voltage minus a small voltage used for the ionisation of the gas in the glass tube. The anode potential can range from 0 kV to 2.5 kV but for about 2 kV and over the plasma discharge tends to be unstable and this disturbance reduces the stability of the ion beam. The accelerator voltage can range from 0 kV to 150 kV.

To invert the beam polarity all the electric fields are reversed except in the ion source itself. The negative ions which emerge must be the result of electron capture collisions between the accelerated positive ions and the residual gas present in the exit canal. This negative beam required somewhat different operating conditions and the ion flux was approximately a few percent of the typical positive ion beam current. Interestingly, the energy of the extracted ions was found to be determined only by the accelerating voltage; we have no satisfactory explanation for this. This

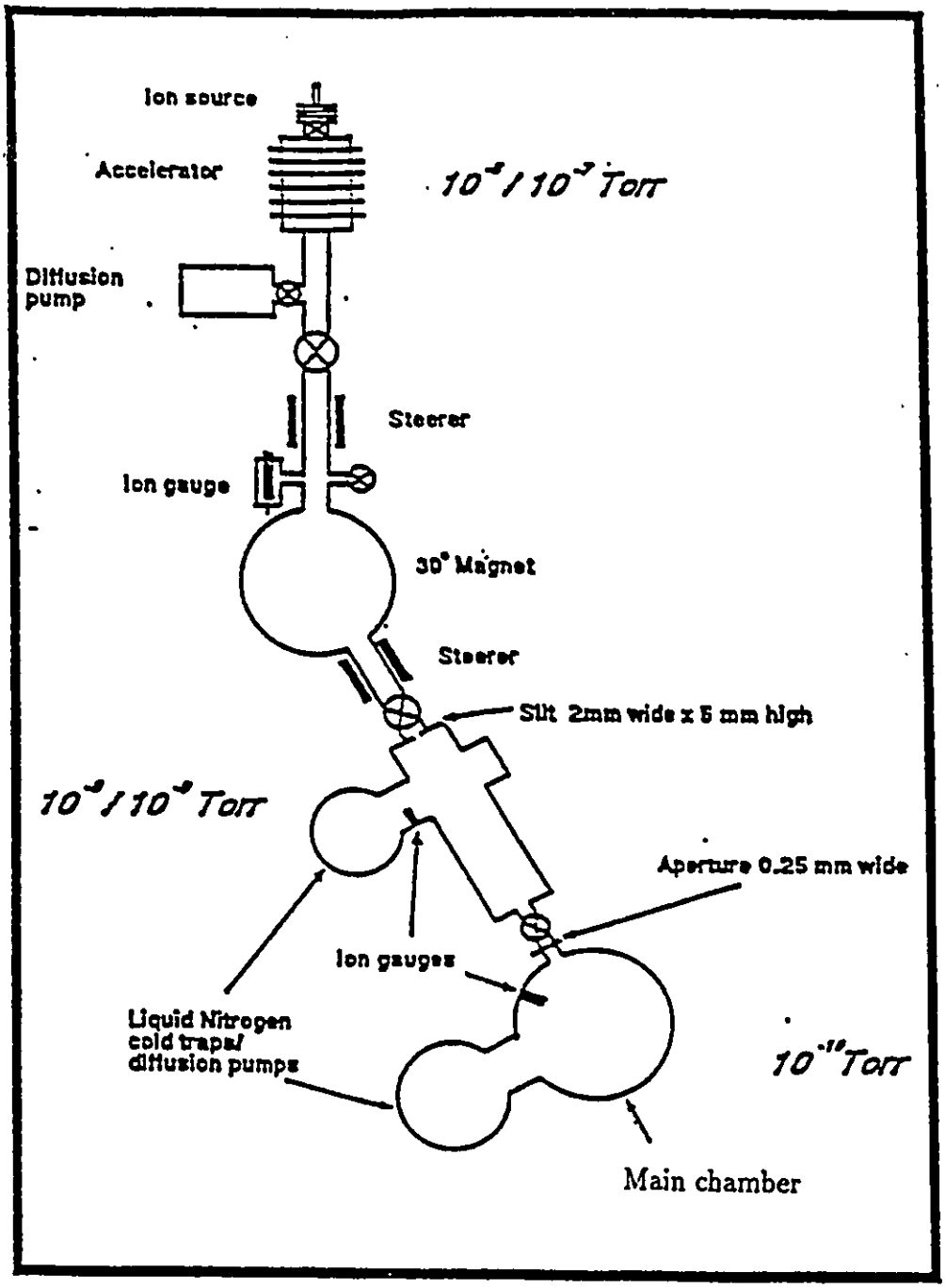

Figure 3.1: Schematic overview of the experimental apparatus

polarity reversal option is an advantage which is not available to many research groups presently engaged in this field of research.

Certain measurements required a low energy beam. The accelerator was designed for $\sim$ 100keV ions and without modification did not produce sufficient ion current at a few keV. By applying a negative high voltage partway along the resistor chain (on the accelerator column), the ion flux was greatly enhanced. This ion production enhancement can be explained as follows: the plasma extracted at an initial energy is accelerated to a high potential which allows a higher extraction efficiency of the ions from the plasma boundary. The ions are then decelerated back to a lower energy in a low gas pressure region where the beam is widely spread so that the space charge effects are small. As a result, the low energy ion beam current was increased by a factor of about 30.

Different ion beams were produced by letting small amounts of high purity gas of the appropriate elements such has oxygen, nitrogen, neon and argon into the ion source bottle. For certain beams we had to resort to using high purity molecular gases; a good intensity C^+ beam was obtained with carbon monoxide while strong P^+ beams were produced by using pure phosphine gas (PH_3) in conjunction with a few grams of phosphorous powder deposited inside the plasma discharge tube itself. S^+ was produced by placing a small quantity of sulphur powder in the source and using argon as a buffer gas. Freon-12 (CCl_2F_2) was used to produce the Cl^+ and F^+ beams.

3.3 Mass selection and beam collimation

The ion beam is deflected by a 30° bending magnet through two narrow slits. The magnet separates out different ion masses by deflecting each mass at a different radius of curvature (Fig.3.2).

A simple relation can be obtained by considering the forces involved for a uniform magnetic field perpendicular to the velocity:

$$\frac{m v^2}{r} = q v B$$

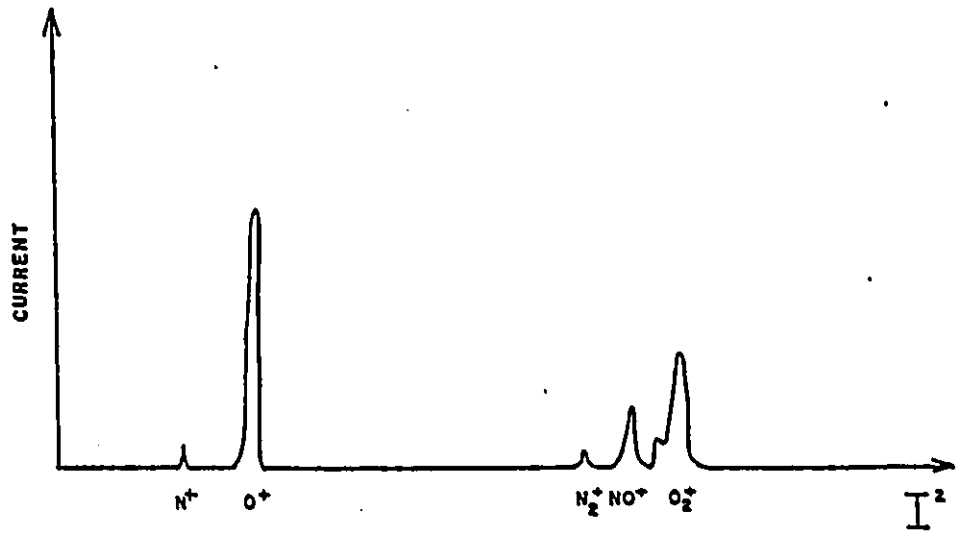

Figure 3.2: Mass spectrum of the ion source. The ordinate represents the current to ground measured on the entrance slit of the main chamber (slit #2) while the abscissa is simply the square of the current (I) sent through the beam bending magnet (as stated in the text, I is proportional to the magnetic field B).

where m, q and v are respectively the ion mass, electric charge and velocity, B is the magnetic field and r the radius of curvature. The velocity can be expressed as a function of the accelerating potential V.

$$E = qV = \frac{mv^2}{2}$$

thus

$$v = \left(\frac{2qV}{m}\right)^{1/2}$$

Combining the first and third equations and rearranging we obtain

$$\frac{mV}{q} = \frac{r^2 B^2}{2}$$

In the right side r^2 is a geometrical constant for all ions which pass through the collimating apertures of the system. All ion mass/charge ratios should therefore lie on the same straight line of a graph of mV/q as a function of B^2.

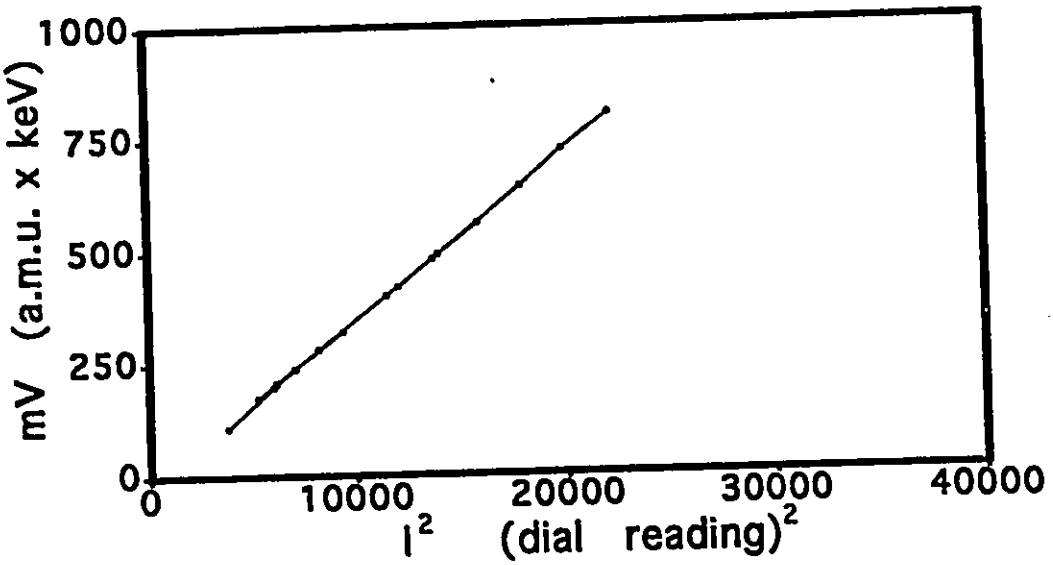

Figure 3.3: Mass calibration graph

The straight line seen on the mass calibration graph (Fig.3.3) was obtained using a well known ion mass (i.e. high purity oxygen in the ion source) for many different accelerating potentials. The other atomic or molecular ions can be determined by interpolation. In practice, the current I through the magnet can be used as a measure of B and the hysteresis effects are kept small by always scanning in the same direction.

Alignment problems through the system were taken care of with the help of adjustable weak transverse magnetic fields perpendicular to the beam line. These "steerers" consist of four coils, wound around a square iron core, surrounding the vacuum pipe through which the ions travel. The coils on opposite sides are connected in series with polarities such that their fields are opposed inside the iron. The return fields emerge from the iron and produce a weak, nearly uniform field in the vacuum. Magnetic fields of a few hundred gauss over a 20 cm path are sufficient to deflect the ion beam by a few degrees. Since the fields are small, there is little iron saturation and the current/field relation is nearly linear. Consequently a change in the left/right deflection, which is produced by a change in the magnitude of the current in the coils on each side (vertical field), does not disturb the up/down

deflection which is produced by the top and bottom coils (horizontal field). Therefore they act effectively as independent controls.

When a careful optimization of all the adjustable parameters was achieved (steerer magnetic fields, ion extraction voltage, ion source gas pressure, anode voltage), sufficient intensity (a few nA on target) could be produced with a wide range of ion beams. The tight geometry of the ion beam after the deflection magnet made adjustment critical. The beam had to be passed through two slits set about 1.2 meters apart. The first slit was 2 mm wide by 5 mm high and the second was only 0.25 mm wide and 8 mm high. This geometry produced a collimated beam that had a narrow energy spread and its angular spread (in the horizontal axis) was about 2 mrad. All ion currents were measured with Keithley picoammeters electrically connected to the slits or the sample in the main chamber, and no correction was applied for secondary electron emission.

Even with all this collimation and focussing action certain beams e.g. F^+ and C^+ were fairly weak especially in the low kinetic energy region (< 5 keV). It was found that there was considerable loss of ions through the very tight geometry of the apertures which defined the differential section. The space charge of the beam itself sets definite limits to ion currents which can be transported as low emittance beams[34]. Calculations showed that we were at these theoretical limits when passing 1 nA through our two slits. To compensate for this space charge increase in the beam size, an einzel lens was placed half way between the apertures of the differential section to refocus the ions. The proportion of ions reaching the target was thereby increased considerably. Additional einzel lenses placed along the beam line did not reduce any further the space charge repulsion of the ions.

3.4 Sample holder

The steady and narrow ion beam hit a target surface (Si(100) wafer mirror-polished) at the centre of the main chamber which was firmly held by molybdenum (Mo) clamps to a Mo holder-plate. The sample holder was commercially made and was found to be unsatisfactory in several ways. It was attached to a high precision

manipulator with X, Y and Z translational movement, rotation about a vertical axis and also rotation in a plane perpendicular to the target normal. The system therefore had five degrees of freedom to accurately position the sample surface.

These sample movements were most easily accomplished when the vertical axis of rotation (the Z axis) was at the surface; with off-axis samples it was more difficult to make the Z axis rotations and at the same time maintain the sample position. The translational resolution of the manipulator was 0.005 mm for all 3 axes. The angular resolution was 0.1° on the primary rotation axis and 0.3° on the secondary axis. The manipulator was equipped with an electron beam heating accessory. This type of heating was provided by an electron emission filament (thoriated tungsten) located directly behind the sample backplate which also acted as a grounded anode. Some thermal radiation heating was produced but this was significantly increased by applying a high negative voltage to the filament to produce about 25 Watts of electron power. This type of heating allowed temperatures as high as 1250°C to be reached very easily.

The temperature of the sample surface could be monitored by means of one or two NiCr/NiAl thermocouples which can be affixed to the sample surface or directly upon the Mo backplate. Note that the negative potential filament produced stray electrons some of which escaped into the chamber where they struck the stainless steel walls and caused surface electro-desorption (primarily hydrogen). This surface outgassing during heating was unacceptable because the pressure rose by a factor 10 at least. The solution was to operate the electron emission filament at ground potential and have the anode positively biased. The stray electrons were then no longer attracted to the chamber walls since they were at the same potential. Unfortunately this arrangement prohibited the use of thermocouples in contact with the backplate (thermocouples operate only near grounded surfaces).

Having the silicon sample in direct thermal contact with the Mo backplate created significant amounts of "hot spots" on the sample i.e. uneven thermal contact between the silicon and the sample holder. This non-uniform thermal contact between the sample and backplate caused several silicon samples to melt during high temperature annealings (e.g. melting point of Si(100) is 1420°C). This problem was

resolved by cutting a square hole slightly smaller than the sample dimensions in the Mo backplate thereby allowing the electrons to strike the back of the sample directly. Not only did this modification prevent the destruction of any more samples, but it also reduced the total power required to anneal our samples because then the sample itself was the hottest part of the system. Another consequence of our modification is that much higher annealing temperatures can now be reached than the commercially specified maximum of 1250°C.

3.5 Energy analyser

A disadvantage of electrostatic analysers as spectrometers for the ions scattered from surfaces is that they scan the ion energy spectrum sequentially. When this is combined with reasonably good energy resolution, the ion beam flux required to produce a spectrum is such that significant surface damage occurs during measurements. The alternative technique, time-of-flight (TOF), collects scattered ions and neutrals of all energies at the same time, and this more than compensates for the smaller solid angle resulting from the large target-detector distances which are necessary for reasonable flight times. TOF spectra have been reported in which the beam dose required to obtain a scattered ion spectrum is $\sim 10^{-4}$ ions/target atom[35, 36]. These ion doses make it possible to perform crystallographic measurements without substantially damaging the surface crystal structure.

A drawback of the TOF method is that without a large vacuum system to contain the distant detector[37] measurements can only be made at certain fixed scattering angles. In addition, as it is usually used, this technique cannot separate out multicharged ions from singly charged ions. This latter drawback, which seems to be present in every TOF system used for surface analysis in operation today, is caused by the design of the apparatus itself. The TOF technique basically consists of a pulsed ion beam which strikes a surface and the emitted particles are velocity analyzed by measuring their flight times from the sample to the detector (typical flight path length is about 1 meter). It is important to note that the detector collects emitted ions as well as neutrals of all energies at the same time with the option of

removing by electrostatic deflection all ions (e.g. both singly and multiply charged ions).

The present system has been designed to increase the detection efficiency to the level where it is possible to obtain spectra without significant surface damage, and at the same time it is possible to make angular distribution measurements inside a small UHV chamber. For ion surface scattering the high energy resolution capabilities of the electrostatic analyser are not required for most surface structure investigations, since usually some proportion of the ions are scattered more than once by surface, or near surface atoms so that the unique energy value predicted from single ion-atom elastic scattering is not observed. Therefore it presents little advantage to use a high resolution spectrometer since the multiple collision events cannot be resolved. It is therefore better to sacrifice energy resolution in order to obtain higher efficiency. The proportion of multiply scattered ions depends heavily on surface structure and differs for each ingoing and outgoing angle.

Measurements requiring scattering angle distributions or the determination of the outgoing ionic charge states can best be accomplished with either an electrostatic or magnetic analyser. Since electrostatic analysers (ESA) are considerably simpler to build and operate than magnetic ones, they are by far the most popular, and this type was chosen for the present system.

There are many different types of electrostatic analysers and their focussing properties have been well discussed by several authors. Two of the most common designs are the 180° and the $\pi/\sqrt{2}$ (or 127°) electrostatic analysers. The former basically consists of two concentric hemispheres: a particle beam enters through an aperture into the space between the two electrodes and is focused to another aperture, directly opposite after a 180° deflection. The main advantage of this type of analyser is that the focussing is in two dimensions; the disadvantage lies in the difficulty involved in accurately machining and constructing the device.

The 127° analyser consists of two cylindrical concentric curved plates separated by a small gap, with entrance and exit slits at an angle of 127°. In addition, this ESA must be constructed entirely from UHV compatible materials such as good quality aluminum and stainless steel for the frame and electrodes. The insulation

for the electrodes is provided by teflon material, but we can also use certain ceramics and machinable glass which are UHV compatible. This analyser is single focussing, since the field is everywhere horizontal; there are no vertical forces and therefore no vertical focussing. It has been shown that ions which have approximately circular trajectories come to a first order focus after they have passed through a deflection angle of $\pi/\sqrt{2}$[38]. Such a focus is not very useful because it lies inside the field region, but if the ions enter and emerge from a cylindrical field region in which their deflection is slightly less than $\pi/\sqrt{2}$, then the source and image points can both be located in field free regions.

The novel design feature compared to previous instruments is that no entrance aperture is used. The separation of the analyser electrodes determines the angle of acceptance in the deflection plane. The space focussing properties of the analyser are such that the bombarded region of the target itself becomes the ion-optic object which is imaged at the exit slit.

The minimum distance at which the analyser can be placed from the target is set by mechanical and practicle constraints rather than by theoretical optimization. The target must have sufficient clearance to move freely without it striking the analyser. Note that the plane of scattering is horizontal, with the incident angle being determined by the vertical rotation axis of the manipulator and the scattered angle by the position of the detector on the horizontal racetrack (see Fig.3.4). For backward measurements, if the analyser is too close to the target, it may intercept the incident ion beam incident. In contrast the image of the analyser may be placed close to the field exit, where for very close distances the exit slit may also usefully act as a field terminator. The present design is based on a target-analyser distance of 15 mm and an analyser-image slit distance of 5 mm.

The energy resolution is simply given by the following equation:

$$\frac{\Delta E}{E} = \frac{(width\,of\,beam\,+\,width\,of\,exit\,slit)}{R_o}$$

With the size of the beam and exit apertures (0.25 mm wide x 5 mm high and 0.5 mm wide for the beam and the exit slit respectively), the theoretical resolution is 1.3%. A convenient test of the analyser was to run the ion beam directly into

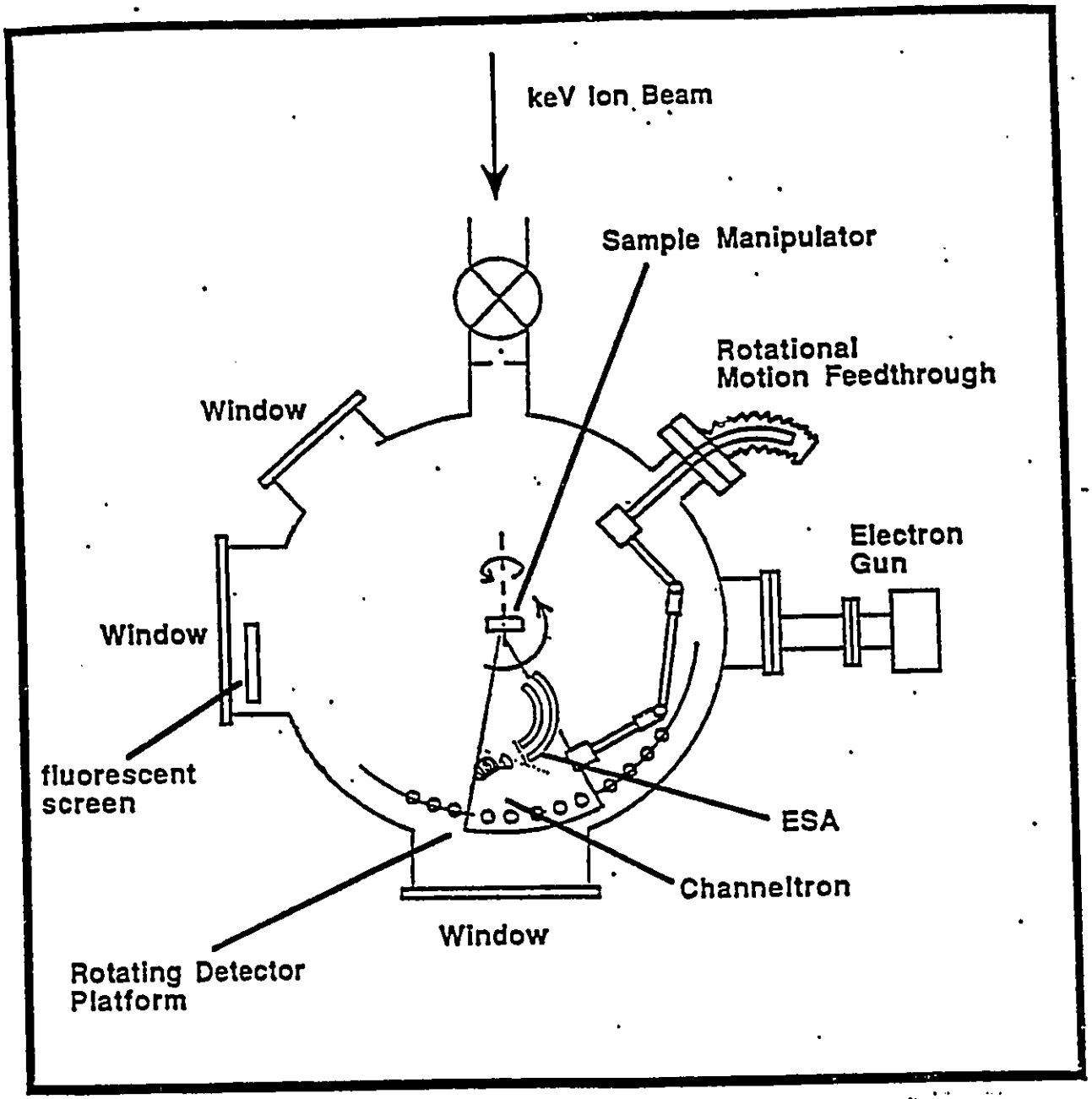

Figure 3.4: Main chamber schematic overview

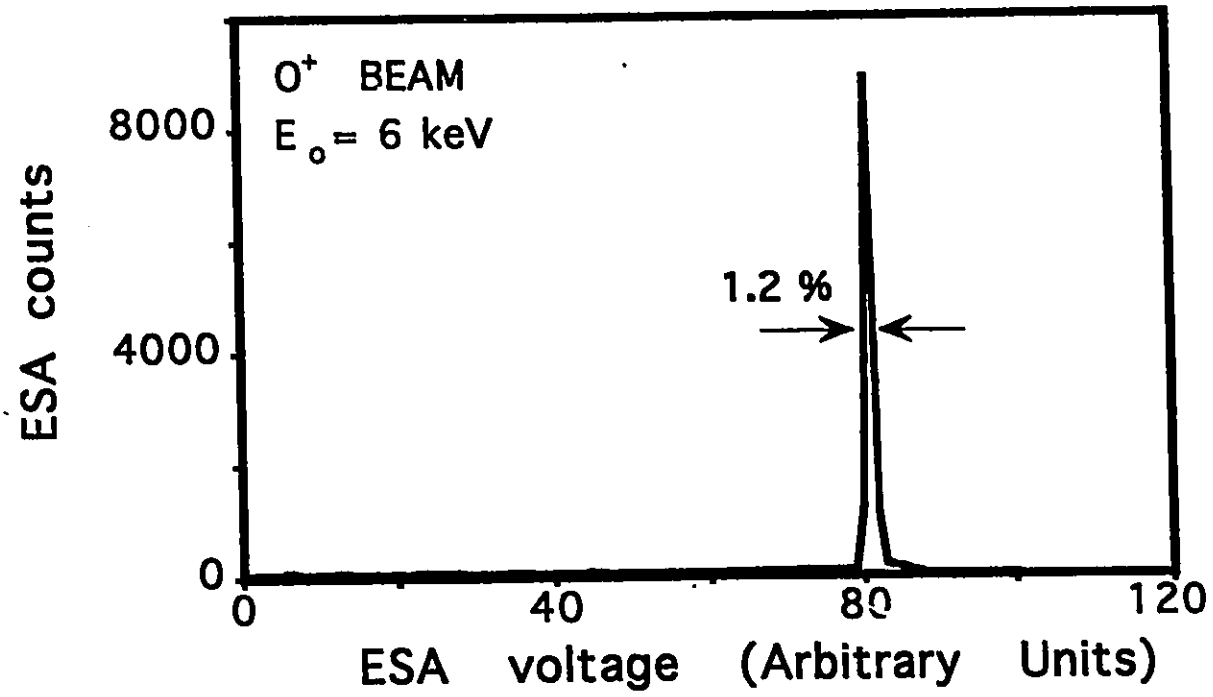

Figure 3.5: Energy spectrum obtained by running an O^+ beam of 6 keV directly into the ESA.

the ESA (Fig.3.5). Note that the beam intensity had to be reduced by a factor of about 1000 to avoid damaging the detector. The beam energy resolution from the magnetic deflection analyser was much better than that of the ESA, so that the beam for this test was effectively monoenergetic.

The energy selected particles which had passed through the ESA were counted individually with a channel electron multiplier (CEM) mounted behind a small slit (0.5 mm wide). The detection efficiency of a CEM for ions has been shown to be independant of energy in the range of 2 to 10 keV[39]. Below 2 keV the sensitivity is lower because the secondary emission coefficient decreases so that the probability that one of the several secondary electrons emitted from the entrance cone following the initial ion impact will be captured and multiplied is less. Above 10 keV the sensitivity is also lower but for a different reason. The ions, possessing more kinetic

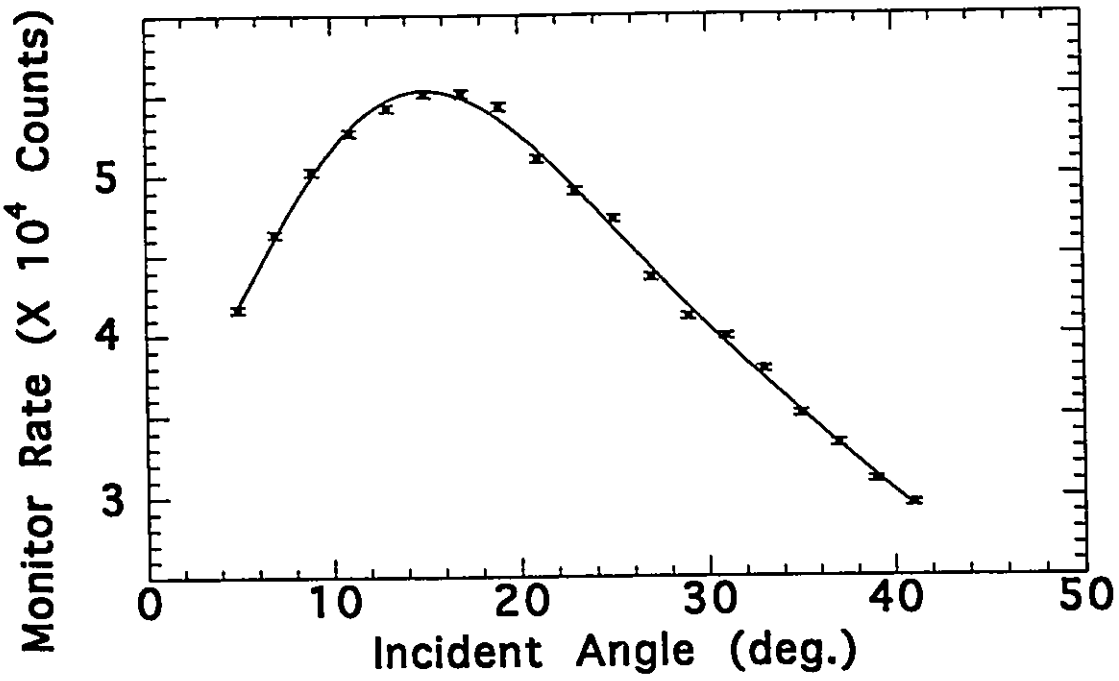

Figure 3.6: Calibration curve for absolute ion yield intensity as a function of target orientation.

energy, have a longer range in solids so that again there is a decreased probability of a secondary electron from the initial impact being emitted and subsequently multiplied.

When the ion beam entered the UHV chamber there was an abundance of secondary electrons emitted throughout the chamber. This electron problem was resolved by negatively biasing to $\sim$200V the front cone of the CEM. This was sufficient to completely repel all the stray electrons resulting from ion scattering. However the negative electrode of the ESA itself was a source of electrons from field emission, and for a sufficiently high operating voltage (on the negative electrode), the stray electrons were again a problem. By increasing the negative bias to the CEM front cone (to about 1 to 2 keV), these higher energy electrons were also repelled.

In addition to the CEM behind the ESA, there was also a second CEM located in the UHV chamber in direct line of sight of the sample just above the beam line

entrance slit ($\theta \sim 180°$). Its sole purpose was to monitor the actual ion intensity on the target during measurements. This method took into account beam fluctuations and in certain cases permitted us to normalise our measurements. This method of ion counting was preferable to measuring the current on the target (since a Faraday cup was not used) because it avoided problems related to the slow response time of picoammeters operating on nA ranges. Another problem was the secondary electron emission effects that occurred during sample heating. The sample would experience a charging up effect with a half-life of several minutes. This slowly decaying charging effect gave quite false ion current readings.

The use of a second CEM to measure scattered ions at $\theta \sim 180°$ as a means to normalise the beam intensity is only valid for measurements where the target is not moved. It has to be modified for measurements of yields as functions of target orientation. Therefore, as a separate experiment, the monitor CEM which counted the total ion yield from the target, was calibrated so that the monitor count for a fixed beam charge was known for each target orientation. The data shown in Fig.3.6 was fitted with a curve and used to normalize the spectrometer counts, as measured relative to the monitor counts, and thus to determine the absolute dependence of each charge state yield on target orientation.

The actual wiring for both CEM's was initially a problem because of the limited number of materials which are UHV compatible. Bare copper wires (Cu is a UHV material) proved to be unsatisfactory because of the electrostatic pick-up between the CEM's involved in having unshielded wires. This problem was solved with teflon coaxial cable (with insulation outside the outer conductor removed). The digital output signals from the two CEM's were changed to low impedance by preamplifiers just outside the vacuum and then sent through coaxial cables to the electronic system where they were amplified and displayed on scalers. These pulses were also fed into a computer for data reduction and storage.

3.6 Reflection high energy electron diffraction

In addition to the ion scattering equipment, the chamber contained an electron diffraction device which enabled us to examine the surface in another way. A low energy electron diffraction (LEED) system could not be used because it must be close to the surface since it requires a large solid angle round the target. The components of the reflection high energy electron diffraction (RHEED) system could be placed outside the main chamber volume, inside the chamber ports, where they did not obstruct the ESA.

RHEED is a technique for surface structure analysis; electrons which are incident upon a flat surface at grazing angle produce a diffraction pattern characteristic of the atomic surface arrangement. Since the normal component of the incident electron momentum is small, the penetration of the electron beam is also small and consequently the information we obtain is from the first few atomic layers of the surface and not the bulk. The electron gun was directed horizontally on an axis perpendicular to the beam and the diffraction pattern was observed on a fluorescent screen located directly opposite the electron gun (on the other side of the target). The electron gun was a commercially purchased device of the type used in cathode-ray tubes (CRT) and the fluorescent screen was taken from an old CRT. Great care must be taken for removal of the fluorescent screen from the CRT; the vacuum seal must be carefully broken and the internal pressure raised gradually up to atmospheric pressure otherwise the fluorescent powder may be blown away and the whole screen ruined.

This RHEED pattern can prove useful for quickly examining the crystal structure of a surface and in some cases identifying the presence of impurities. However, it has been found that ion scattering is a more critical test for hydrogen and carbon build-up.

3.7 Sample preparation

The importance of a clean sample for surface studies is fundamental for these measurements. Prior to inserting our Si(100) sample into the UHV system, it was treated with an oxidation process. We are grateful to the Microstructures Laboratory at NRC for both providing the samples and performing the oxidation. This process consisted in putting the silicon wafer in an oven while exposing it to an ozone gas for about an hour. It is estimated that an oxide layer of about $0.1\mu m$ thick was produced in this way. This ozonated layer completely hid the features in the energy spectrum except for the hydrogen recoil peak. It was easily removed by heating (temperature of about 850°C) since SiO has a higher vapour pressure than Si. The surface contamination was assumed to be emitted with the oxide, leaving a previously internal layer as the new surface. This cleaning procedure was later found to produce a surface cleanliness identical to that which was obtained by simply sputtering and annealing.

For repeated measurements and following overnight exposure to the residual gas, the target was recleaned by 500 eV argon ion sputtering (2 μA/cm^2), for 15 to 30 minutes depending on the contamination present. It was then heated sufficiently (approximately 500°C for 10 seconds) to outgas the surface argon. After this time most of the argon implanted during the sputtering was desorbed, as indicated by the return of the pressure, and the residual gas composition, to its value before heating. This heating was not sufficient to anneal the surface back to a single crystal[40] and it produced an amorphised surface with a RHEED pattern that showed no diffraction spots. The ion scattering spectrum (Fig.3.7 a)) showed a clean silicon surface peak but with no channeling effects at all. Heating the sample to about 900°C for 15 minutes returned the surface to a Si(100) single crystal and produced a clear Si(100) 2 × 1 RHEED pattern. The energy spectrum taken in a non-channeling direction (Fig.3.7 b))was identical to the amorphised surface.

Following about 48 hours of exposure to the residual gas (2.5×10^{-10}torr), the energy spectrum (Fig.3.7 c)) showed a growing oxygen contamination peak (oxygen beam/oxygen target atom). For a residual pressure of 2.5×10^{-10}torr, Langmuir's

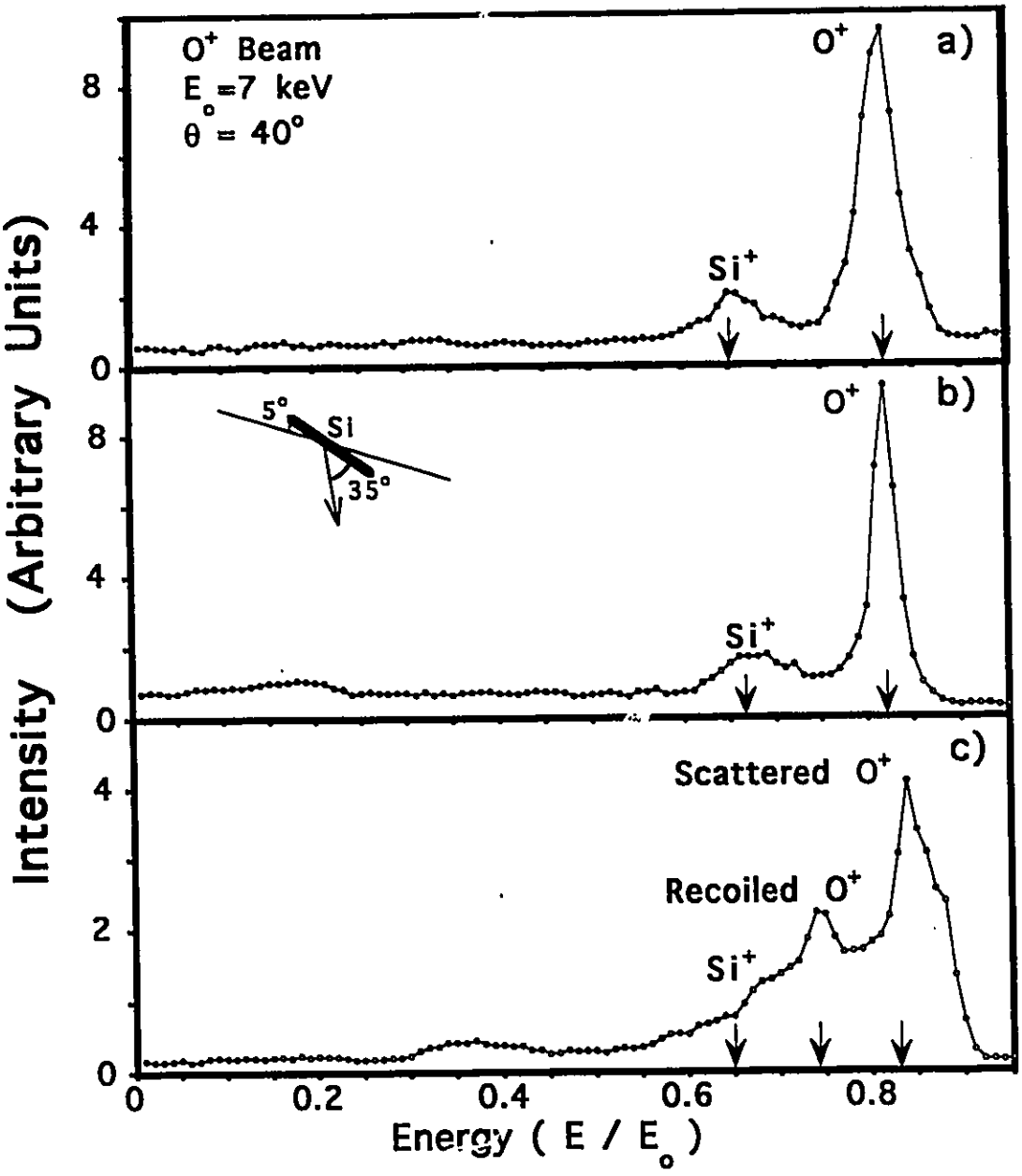

Figure 3.7: Energy spectra obtained by scattering 7 keV oxygen ions, incident at 5° to the silicon surface, into a detector placed at a forward angle of 40° to the incident beam. Figure a) shows an amorphized surface while b) is a single crystal surface and c) is an oxygen contaminated surface.

equation predicts that one monolayer of atoms will stick to the surface every 4000 seconds assuming a sticking probability of unity.

For charge exchange measurements, an amorphous surface was chosen so as to avoid the anisotropies produced by shadowing and blocking effects in a single crystal. These are known to influence the emitted ion charge states[20, 41]. During ion bombardment, surface damage might change the surface structure of a single crystal, and so change the scattered and recoil ion yield in certain directions.

To test the amorphous condition of the target, the variation of scattered peak intensities was determined as the target was rotated in its own plane. An angle of incidence to the surface of 5° was chosen, as being well inside the shadow cone angle of adjacent surface atoms. No statistically significant variation was found. Repeating this measurement with the fully annealed Si(100) single crystal surface showed the expected decrease in intensity along the (110) direction (Fig.3.8).

Carbon is considered one of the more difficult elements to remove from a silicon surface, and is often a serious contaminant. However, it has been reported that islands of SiC can be removed by sputtering though not by heating[42]. Carbon can be present in the residual gas, a consequence of using oil diffusion pumps, but this should be a negligible amount. Certain measurements were performed with an incident carbon beam but special care was taken that such contamination did not affect the data. Each scan of the energy spectrum took about 5 min, compared to about 2 hours for the beam to strike every surface atom, so that by sputter cleaning the surface after every few measurements the carbon build-up from the beam on the surface was negligible. The measurements showed no indication of a peak in the energy spectrum where C^+–C scattering would be observed.

To determine the effect on the data of surface contamination by carbon, tests were made without sputter cleaning between measurements. The main change was found to be a decrease in the scattered ion peak areas, with a smaller decrease in the recoil ion peaks, and a slight increase in the background. The different charge states were affected about equally, so that inadequate sputter cleaning would not significantly change the ratios of the peak areas. No similar reduction in peak intensity was found for any of the other different beams used in this work.

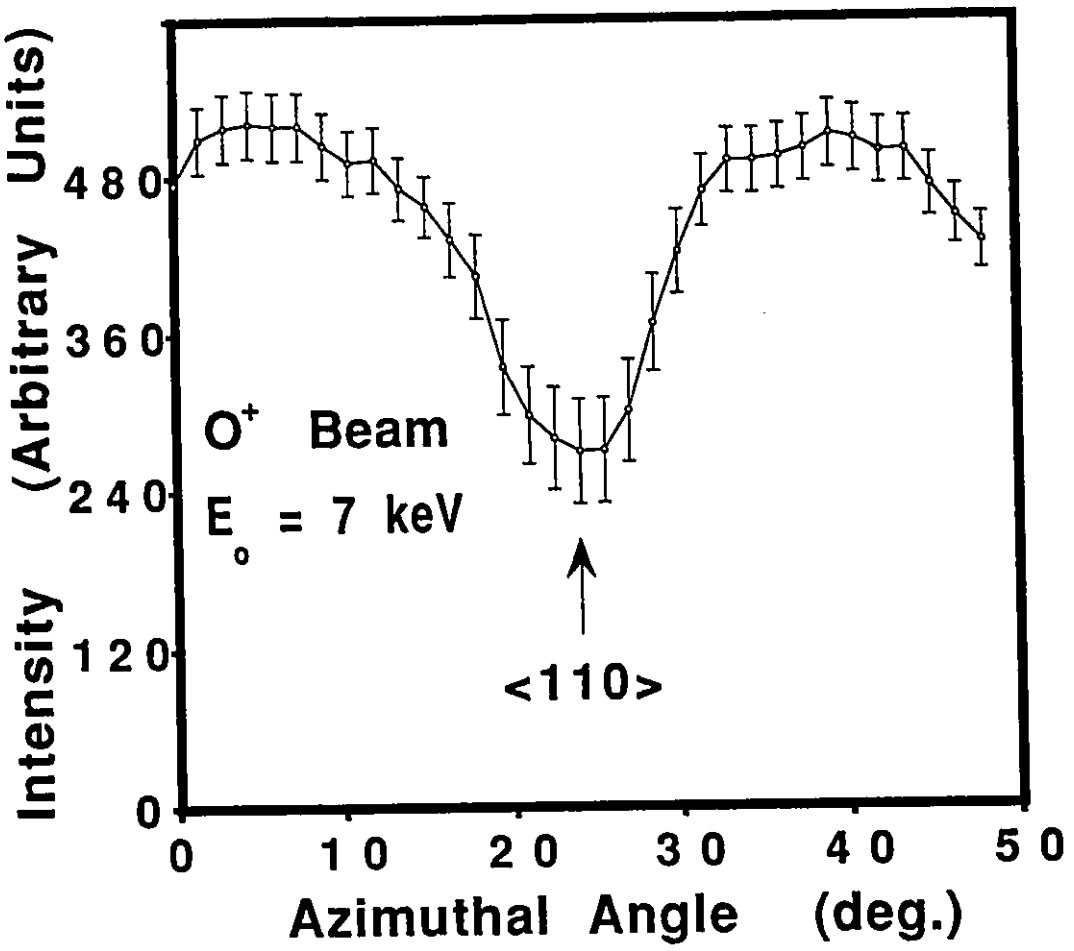

Figure 3.8: Surface shadowing and blocking pattern obtained from a clean Si(100) 2×1 crystal measured with 7 keV oxygen ions as projectiles. The dip shows the expected decreased intensity when the beam is aligned with the $\langle 110 \rangle$ symmetry direction.

Chapter 4. Experimental results

4.1 Energy spectra

Fig.4.1 shows energy scans obtained with projectiles of lower atomic number (Z_1) than the target ($Z_2 = 14$). All the peaks can be identified as binary collision events, and the energies agree well with collision kinematics. Note that to follow the same path through the analyzer, doubly and triply charged ions require half and one third respectively of the deflection voltage of singly charged ions. The peaks which are labelled as doubly charged occurred at voltages exactly half (to one channel) of the singly charged peaks, and one third for the triply charged ions. As a verification that these were indeed multicharged ions, measurements were repeated over a range of scattering angles. Throughout, the ratio was found to be constant, whereas it would have changed if we were observing recoiling singly charged ions from heavy atom surface impurities which would have appeared in this region of the spectrum.

As explained earlier, ions which have made two or more small angle collisions with surface atoms may have more energy than those where the same total deflection is produced in a single collision. Such events appear as shoulders on the high energy side of the peaks. This multiple collision shoulder of the scattered peak was subtracted when estimating the yield of ions which had made single collisions.

The proportion of multiply scattered ions is found to increase with Z_1, and is most evident for Ne^+. To exclude multiple scattering for this extreme case, the usual linear interpolation method for background subtraction was not used to estimate the SS intensities. Instead, a gaussian distribution of adjustable height, width, and position was subtracted from the peak region until a monotonic background underneath was obtained. As a check this gaussian method, which was necessary to obtain the singly charged Ne^+ peak area, was compared to the areas derived from simple linear interpolation on all the other energy spectra. The energy scans

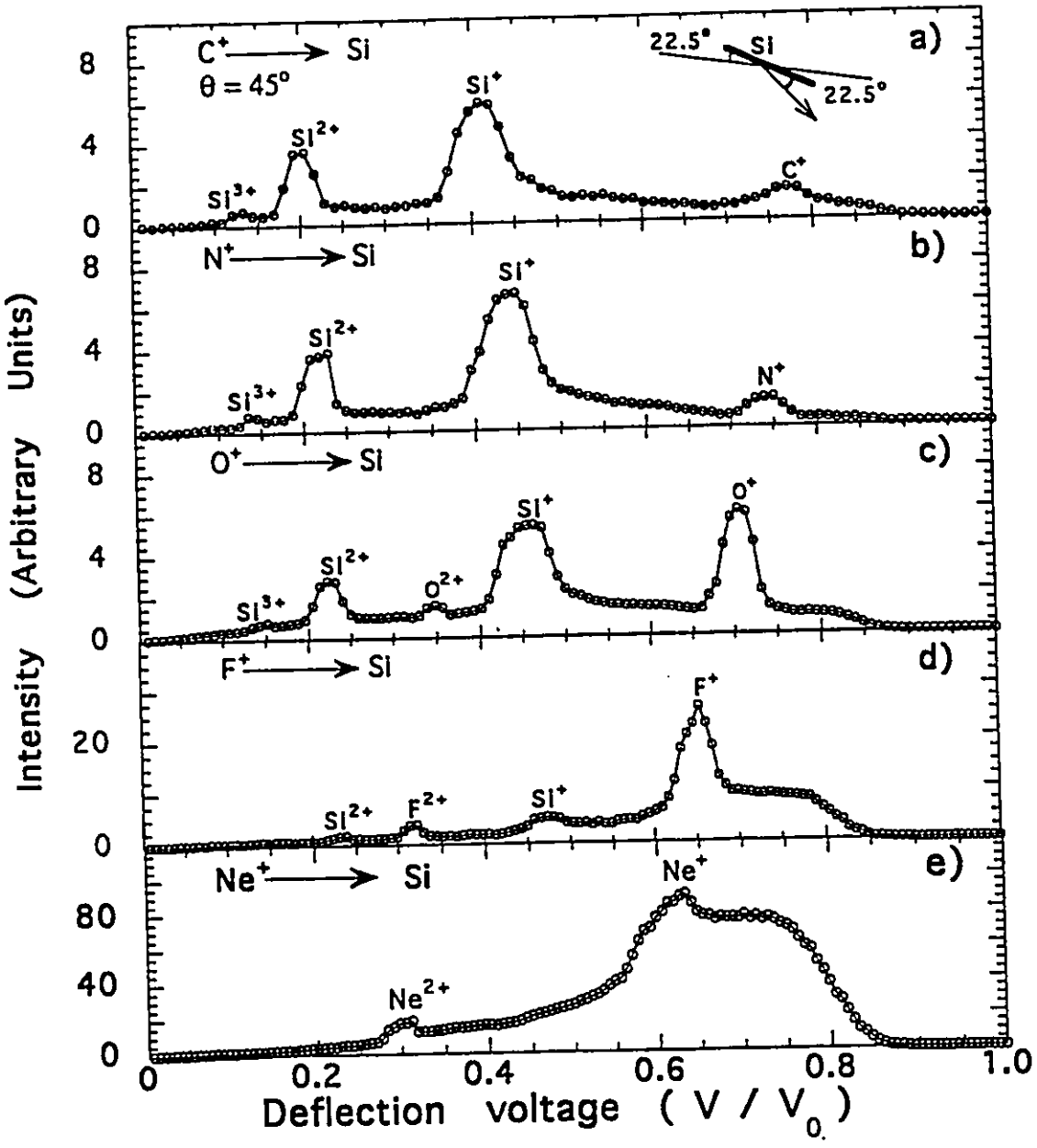

Figure 4.1: Electrostatic analyzer (ESA) spectra of ions emitted at $\theta = 45°$ to the incident ion direction from a clean silicon amorphous surface. V is the deflection voltage, and V_0 is the voltage required to deflect the direct incident ion beam through the ESA. The same incident ion velocity 0.53 keV/amu was used for all the measurements. The incident beams were (a) C^+; (b) N^+; (c) O^+; (d) F^+, and (e) Ne^+.

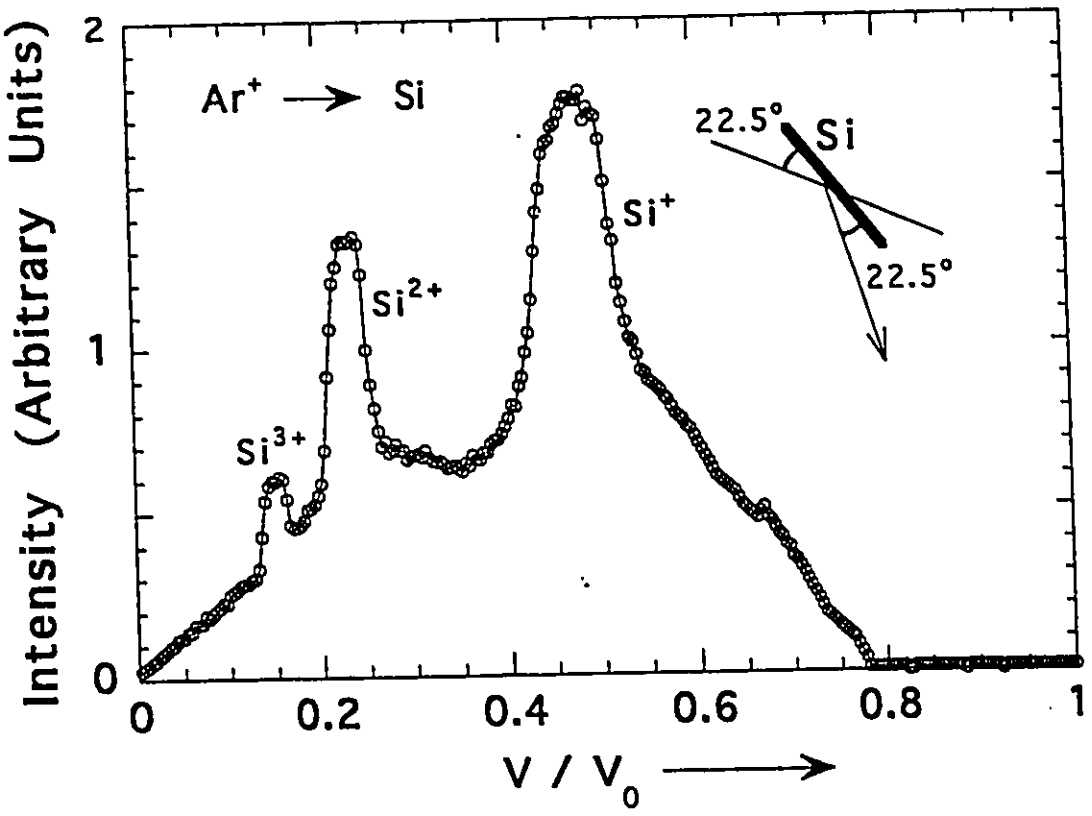

Figure 4.2: Energy spectrum obtained from scattering Ar^+ ions from silicon

we obtain by using projectiles of higher Z (15, 16, 17, 18) than the silicon target showed the same features. P^+, S^+ and Cl^+ ions gave very similar spectra to that of Ar^+ with very strong recoil peaks (singly, doubly and triply charged) and very small singly charged scattered peaks. For this reason Fig.4.2 only shows one energy spectrum, that of Ar^+–Si scattering. Besides the multicharged recoil peaks, no scattered multicharged ions were detected.

4.1.1 Error analysis technique

The ion yields used in this work were obtained by summing the counts in the peak of the energy spectra after subtracting the background, which was estimated by linearly interpolating the intensities on either side. Since the statistical errors can be made

Table 4.1: Statistical uncertainties associated with each channel in a typical yield determination

Channel number	ESA channeltron counts ($\times 10^4$counts)	Beam monitor channeltron counts ($\times 10^4$counts)	ESA counts / Beam monitor counts	Statistical uncertainty (%)
18	1.821	12.17	0.1496	0.80
19	1.749	11.92	0.1467	0.81
20	1.672	11.99	0.1394	0.83
21	1.723	12.26	0.1405	0.81
22	1.724	12.04	0.1432	0.81
23	1.974	11.85	0.1666	0.77
24	3.104	11.88	0.2613	0.64
25	5.103	12.09	0.4221	0.53
26	6.844	12.27	0.5578	0.48
27	6.710	11.67	0.5750	0.48
28	5.543	11.92	0.4650	0.51
29	3.556	11.34	0.3136	0.61
30	2.532	11.62	0.2179	0.69
31	2.225	11.48	0.1938	0.73
32	2.317	11.77	0.1969	0.72
33	2.342	11.54	0.2030	0.72
34	2.397	11.37	0.2108	0.71
35	2.472	11.98	0.2063	0.70
36	2.499	11.85	0.2109	0.70

small (as seen in Table 4.1), an estimate of the error inherent in each spectrum can be found by taking two extreme hypothesis for the background and calculating the yield for each. Typically six points on either side of the peak were taken to estimate the background and two straight lines were drawn as shown in Fig.4.3 to demonstrate the two extreme scenarios. For the peak shown in Fig.4.3 the error was estimated at about 8%, which was typical for many of our spectra. However, this method became less accurate when small peaks were evaluated, particularly when a multicharged ion peak approached its energy creation threshold since the peak in the energy spectrum became indistinguishable from the background fluctuations.

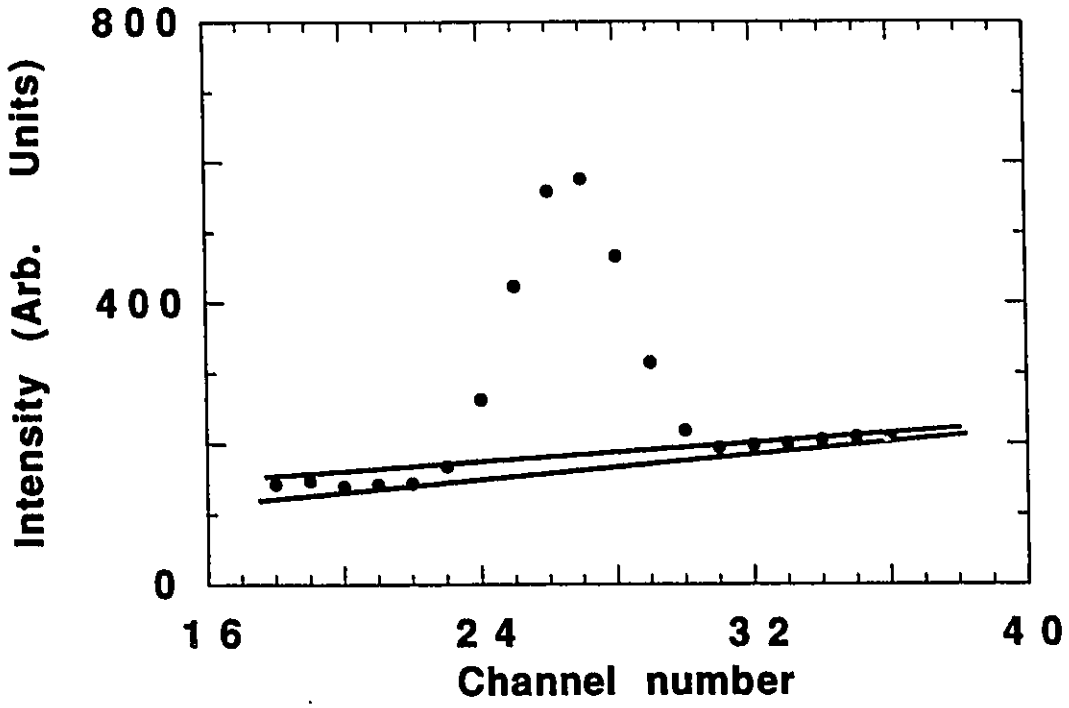

Figure 4.3: Error estimate technique for a typical peak in the energy spectrum

The solution was to concentrate our scan on a small portion of the spectrum and to increase the detection time per channel since we accurately knew over what channels a multicharged ion peak would appear. This procedure reduced the background fluctuations to an acceptable level (less than 1% fluctuation in many cases) and allowed small multicharged ion yields to be discernable and evaluated with sufficient accuracy. For example, the O^{2+} ion yield was evaluated at 0.19 ± 0.06 when 5.8 keV O^{+} ions were scattered at 40° from a Si target, which is just above the O^{2+} energy creation threshold. Note that the appearance of a multicharged ion peak was judged to be valid when multiple scans at the same energy repeatedly gave a positive yield value. As a verification of the validity of our results, measurements were always repeated at a later date, at least once, sometimes twice.

The determination of the energy creation thresholds was perhaps the most subjective part of this research since at least two large sources of error came into play.

First, the actual energy of the incident particles was not absolutely known because the plasma discharge was not monoenergetic (an estimate of the energy anisotropy would be about 30 volts) and the power supply calibration was accurate to about 40 volts. Secondly, deciding at which energy a multicharged ion peak appeared required some personal judgement on the part of this researcher (about 100 volts of uncertainty).

4.2 Ion yield variations with beam energy

The energy variations of the intensities of the ions scattered or recoiled from the surface at 30° when O^+ ions are incident at 10° (40° deflections) are shown in Fig.4.4 and Fig.4.5, respectively. Because of the increase in multiple collisions and subsurface scattering which generates a continuous energy background, a high energy limit to the measurements (30 keV) was arbitrarily set. A procedure to normalize the count rates to the beam current was possible for the target tilting measurements described in the next section, but this method fails when the kinetic energy of the incoming ions is varied because of possible variations in the monitor normalization. This effect probably varies slowly so that the general features of our figures should be valid. The same type of energy variation was found using N^+ projectiles instead of O^+.

The rise with increasing energy which occurs for singly charged ions requires some explaining since the binary scattering cross section at a fixed scattering angle decreases with increasing collision energy. Two effects may contribute to the increased yield with increasing energy: a decrease in shadowing and a decrease in neutralization[43]. Shadowing of a surface atom occurs when it lies within the shadow cone of a neighbour. It is possible to make an estimate of the amount of shadowing by making some simple assumptions about the average distances between nearest neighbours on the amorphous surface.

We assume that no two atoms on the amorphous silicon surface are closer than the nearest neighbour distances on a Si(100) surface of 3.8$\mathring{A}$. Calculations of two-body collision trajectories[6] using the screened Coulomb potential in the "universal"

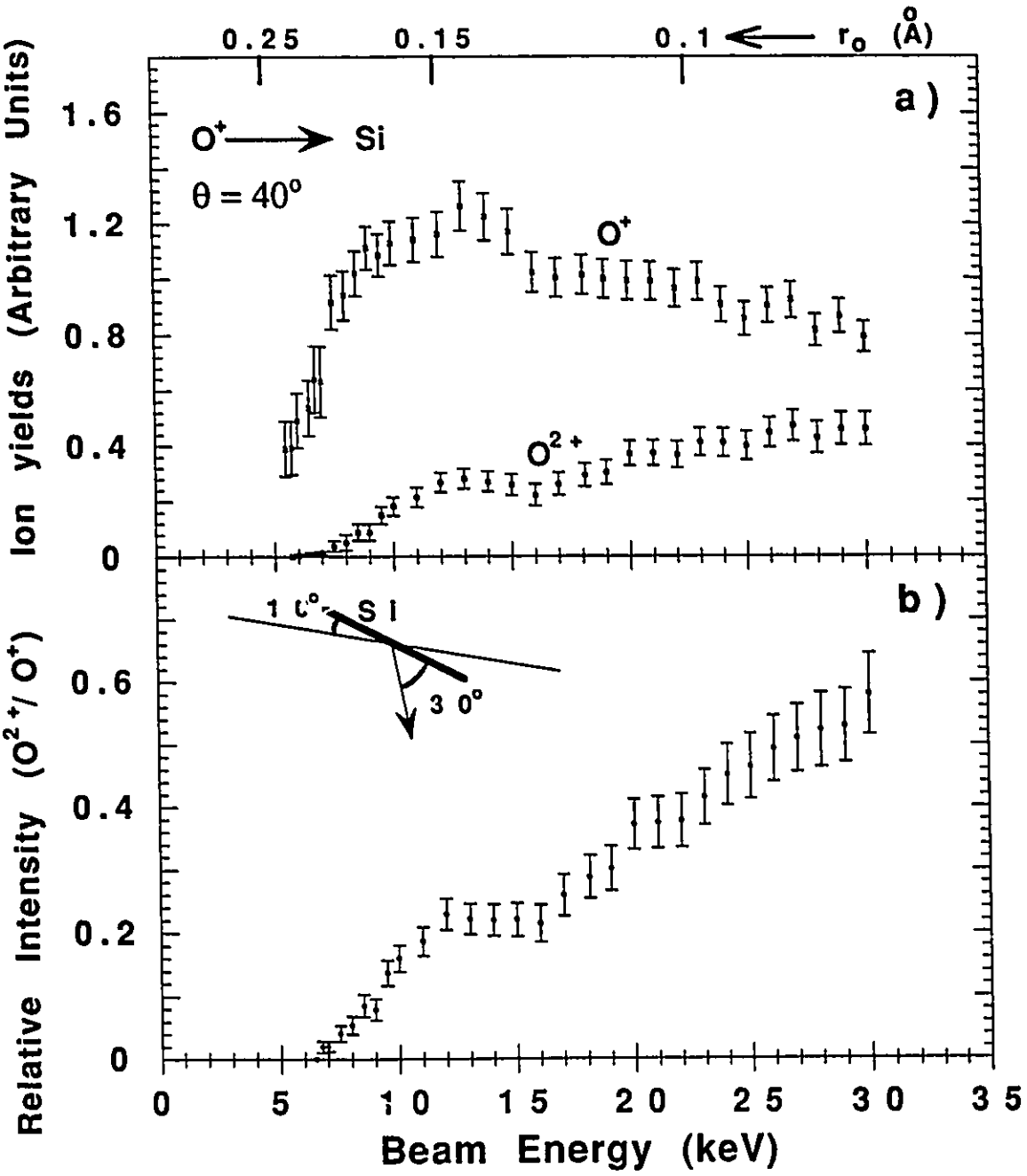

Figure 4.4: The energy dependence of singly charged and doubly charged oxygen ions emitted at 30° from a clean amorphous silicon surface when O^+ ions strike the surface at 10°; graph a) O^{2+} and O^+ yields; graph b) the ratio of yields O^{2+}/O^+.

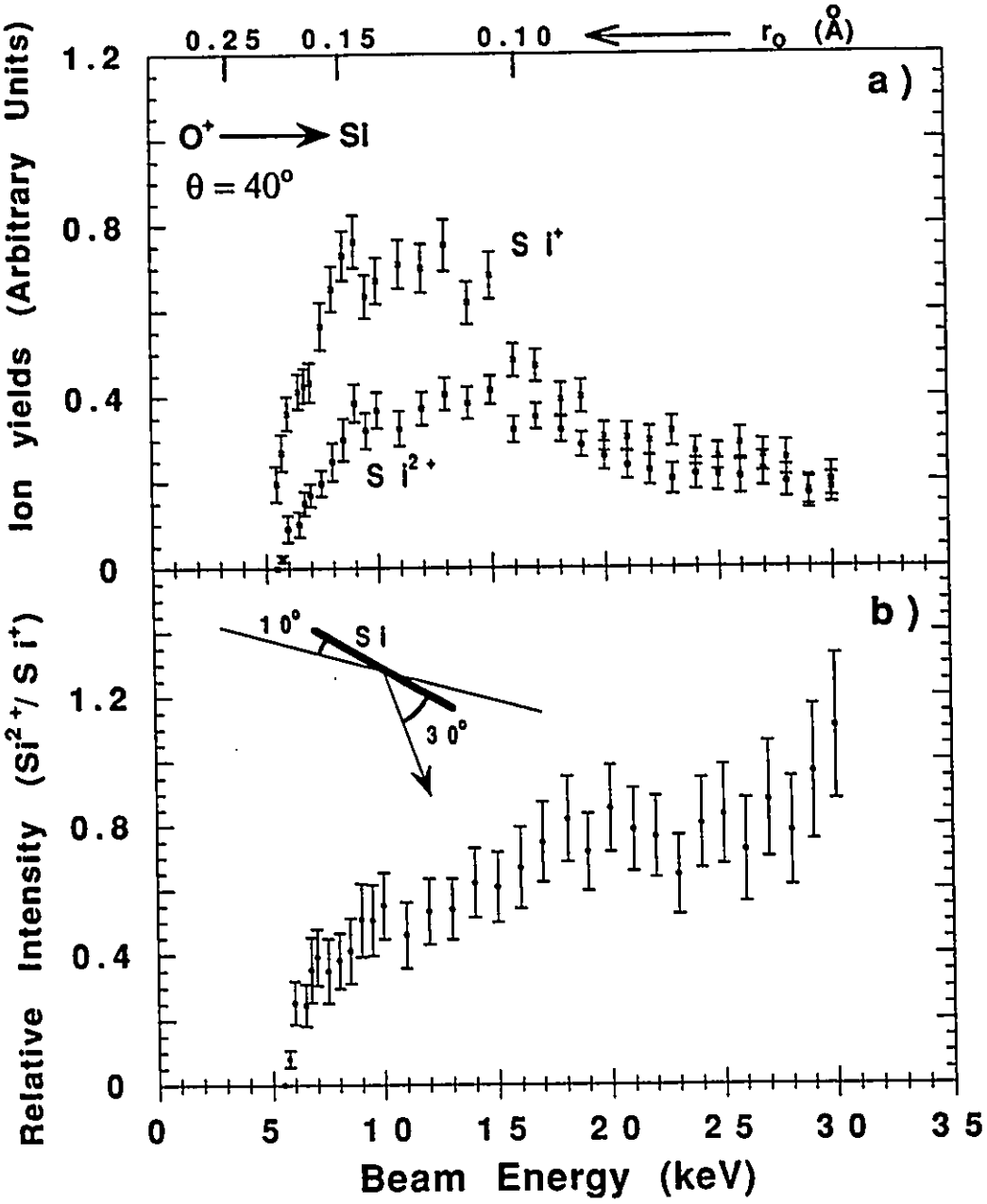

Figure 4.5: The energy dependence of singly charged and doubly charged recoil silicon ions emitted at 30° from an amorphous silicon surface when O^+ ions strike the surface at 10°; graph a) Si^{2+} and Si^+ yields; graph b) the ratio of yields Si^{2+}/Si^+.

form given by O'Connor and Biersack predict that the shadow cone behind each surface atom at 3.8Å separation has an angular width of 10° for 14 keV ions. This is the angle of incidence of the ions to the surface, so that at energies above 14 keV, where the shadow cone angles are smaller than 10°, all the surface atoms are accessible to the beam and shadowing should be negligible.

As the ion energy is decreased, the shadow cone angle expands and the atoms become shadowed by their neighbours. If we further assume that the majority of surface atoms are closer spaced than the lattice constant 5.43Å, then at an ion energy where the shadow cone reaches 10° at a spacing of 5.43Å the majority of the surface atoms will be shadowed and the scattered ion yield will be very small. Trajectory calculations show that this occurs for 6 keV ions. At lower beam energies a larger atom separation is required. For example, surface atom scattering at 2 keV can only occur if the atom has no neighbour within 7Å. Surface roughness should tend to decrease shadowing effects, so that these limiting energies are probably overestimated.

The small yields of O^+, N^+ and Si^+ ions which we observe at low energies are thus from the relatively few atoms on the surface which have these larger than average separations from their neighbours. This simple shadowing model therefore fits the decrease to a small value at our lowest energies and the maximum yield in the energy range below 14 keV. The increase in the neutral fraction presumably also contributes to the decrease at lower energies.

Shadow cone effects decrease the yield of doubly charged ions in exactly the same way as they decrease the yield of singly charged ions. However we observe a definite fall of the doubly and triply charged ions to undetectably small values at energies where there is still a significant yield of singly charged ions. Thus a real threshold exists for the creation of these multiply charged ions independent of shadowing and it therefore must be associated with individual ion-target atom collisions and subsequent surface neutralization effects.It is possible to cancel out the effects of shadowing by taking the ratio of the multiply charged ion counts to the singly charged ion counts shown in Fig.4.4b) and Fig.4.5b).

Based on the assumption of charge independent shadow cones, our measured ratios of ion counts can be interpreted as the relative probability that a particular incident ion which collides with a surface atom will exit this surface and result in a doubly or singly charged ion. This assumption was put forth by Van Der Weg and Bierman[20] who attributed the differences which they observed in the shadowing and blocking angular distributions to different decay rates of the ions with different charges as they pass near neighbouring atoms on the way out.

4.3 Neutralization effect during the outgoing trajectory

If it can be assumed that multicharged ions are only produced at close encounters with individual target atoms, at separations much smaller than the atomic spacing, then the numbers of multicharged ions which are produced there by ion scattering in the solid should be substantially independent of the structural properties of the surface, neglecting shadowing effects of the incident ions. The amount of electron promotion occurring should depend only on details of the trajectory in the neighbourhood of the close encounter and so depend only on the scattering angle (θ) and the ion energy. Once created, the proportion of these ions which escape from the surface without change in their charge depends on interactions with neighbouring atoms and with the average surface potential. A measurement which keeps the scattering angle and the ion energy constant also keeps the distance-of-closest-approach constant and with it the fractions of multicharged ions created at the close encounter. Any variation of the charge fractions as a function of the angle ϕ_{out} of the surface to the emitted ions therefore selectively investigates the outgoing interactions as the ions leave the surface.

Fig.4.6 shows the scattered yields of O^+ and O^{2+} ions plotted on a logarithmic scale as a function of v^{-1}, where $v = v_o\, sin(\phi_{out})$, which is proportional to the time spent in the outgoing region. The time was varied by changing the exit angle ϕ_{out} while keeping all other conditions constant (40° scattering angle, 10 keV beam, 7.58 keV scattered ions).

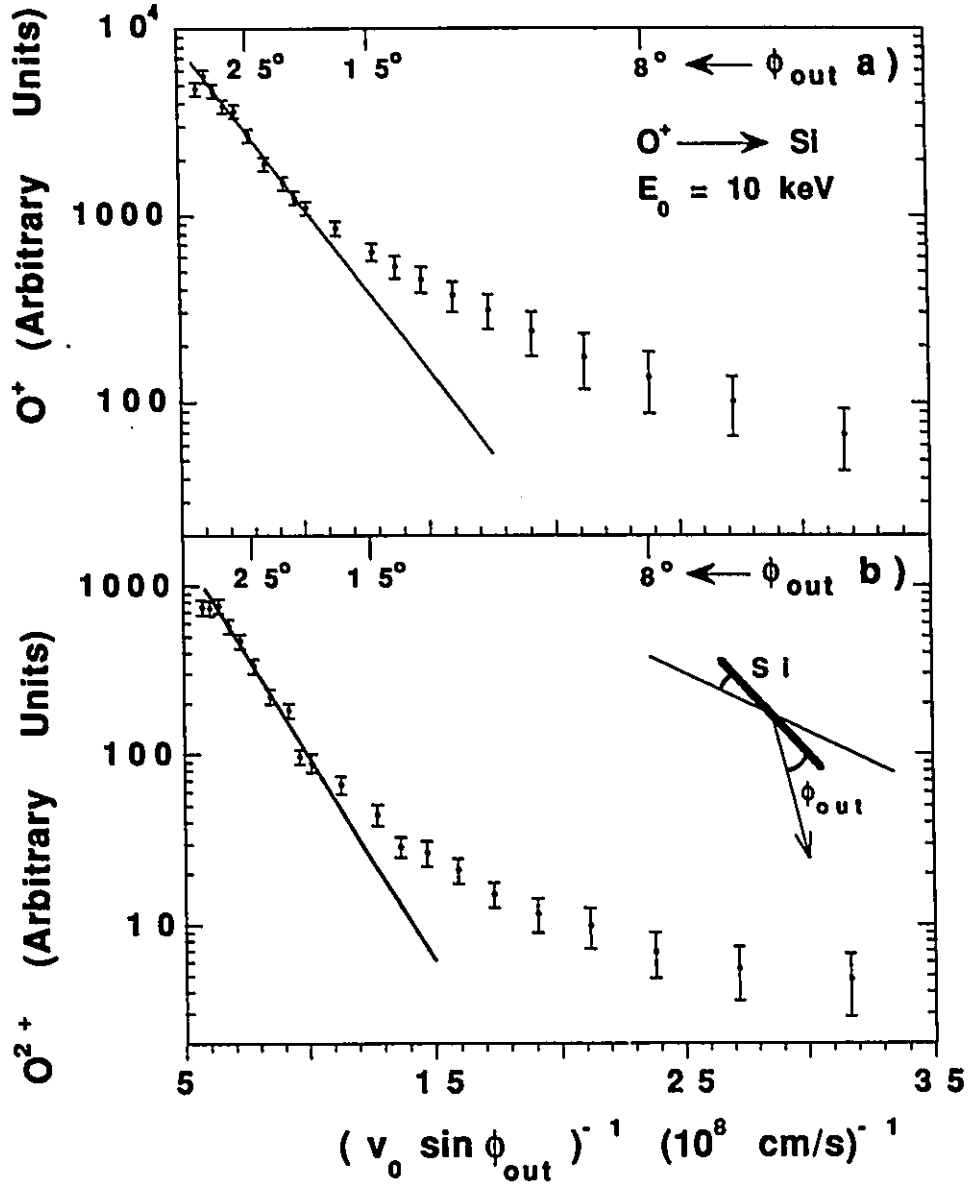

Figure 4.6: The effect of tilting the target while maintaining constant beam energy and scattering geometry. Scattered ions are detected at a fixed angle of 40° to the 10 keV O^+ incident beam. The exit angle ϕ_{out} is varied so that $v_o \sin \phi_{out}$ is the component of the ion velocity perpendicular to the surface; graph a) O^+; graph b) O^{2+}. The lines are theoretical predictions assuming characteristic velocities $A_2/a = 5.5 \times 10^7$ cm/s and $A_1/a = 4 \times 10^7$ cm/s.

As mentioned earlier, Hagstrum assumed a transition rate ($R(s)$) for surface neutralization of the form $A\,exp(-as)$ where s was the perpendicular distance from the surface and A and a were constants.

The transition rate is defined by

$$R(s) = -\frac{1}{P_s}\frac{dP_s}{dt},$$

where P_s is the population of the state. A solution to the differential equation is

$$P_s = \frac{exp\left[\frac{A}{av}e^{-as}\right]}{exp\left[\frac{A}{av}e^{-as_o}\right]}$$

where the ions start at s_o, so that $P_{s_o} = 1$. When $s_o = 0$

$$P_s = exp\left[\frac{A}{av}\left(e^{-as} - 1\right)\right],$$

and when $s = \infty$

$$P = exp\left[-\frac{A}{av}\right].$$

Simply stated, the survival probability for an ion to leave the surface unneutralized is proportional to $exp(-A/(av))$. Since v is the ion velocity component perpendicular to the surface, the ratio of the two constants (A/a) which parametrize the transition rate is thus a characteristic velocity for the decay of singly charged ions to neutrals as it traverses the surface region. The same formalism can be applied to multiply charged ions, so that (A_2/a) can be defined as the characteristic velocity for decay of doubly charged ions into singly charged ions during their passage out through the surface.

A similar analysis was performed on the recoil Si^{3+} and Si^{2+} ion data shown in Fig.4.7 taken under the same experimental conditions (68° scattering angle, 10 keV beam, 5.43 keV recoil ions). The theoretical exponential dependence on v^{-1} is derived assuming the decay of one charge state only. In our data the Si^{2+} ions are almost as intense as the Si^{+} ions so that some account should be taken of the component in the Si^{+} ion yield data which is the result of Si^{2+} decay after the close encounter on the way out. Only for the Si^{+} data shown in Fig.4.7c) is this cascading

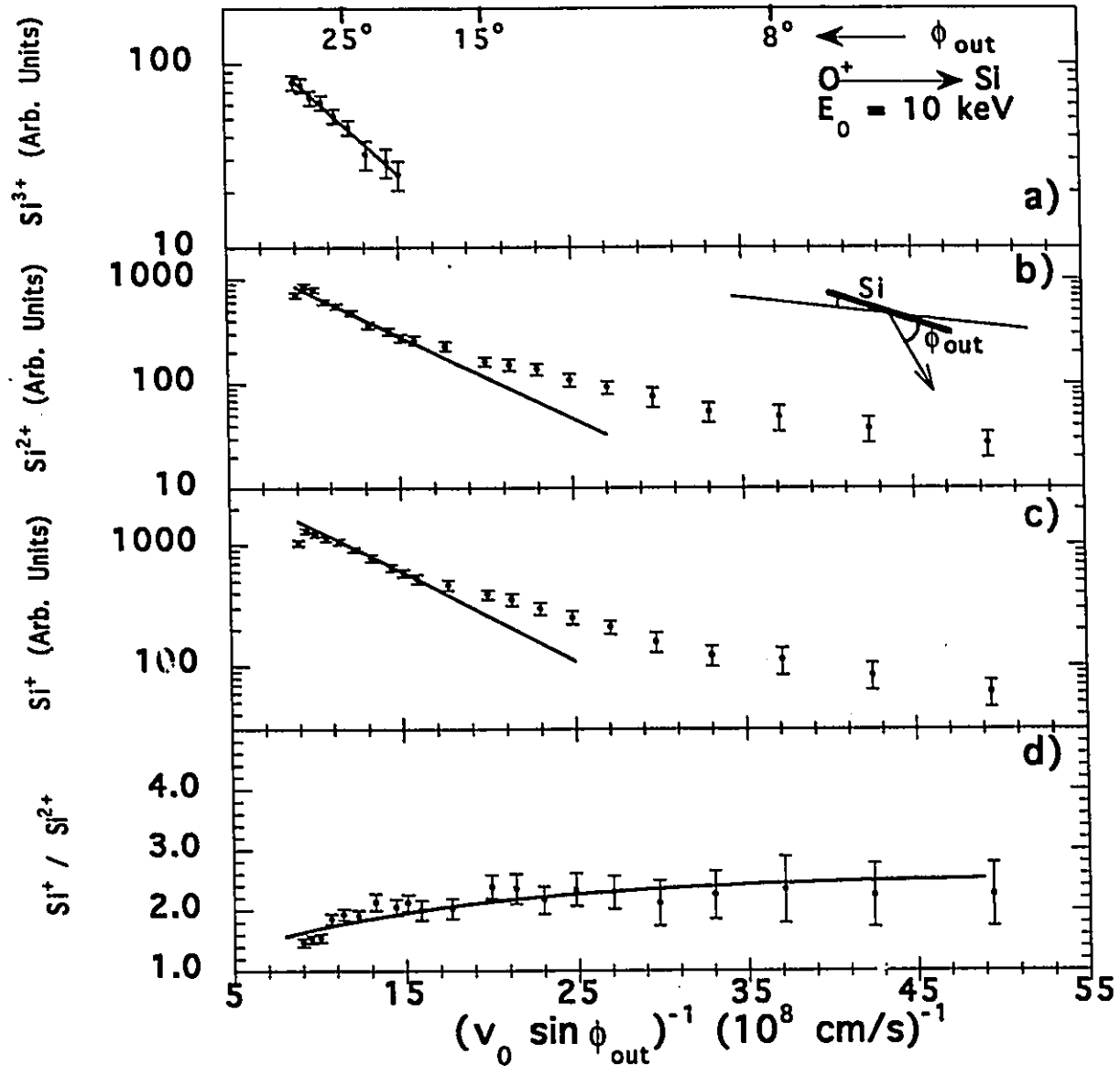

Figure 4.7: The effect of tilting the target while maintaining constant beam energy and scattering geometry. Recoil ions are detected at a fixed angle of 40°; graph a) Si^{3+}; graph b) Si^{2+}; graph c) Si^+; graph d) Si^+/Si^{2+}. The lines are the theoretical predictions assuming characteristic velocities $A_3/a = 2.4 \times 10^7$ cm/s, $A_2/a = 1.8 \times 10^7$ cm/s, and $A_1/a = 2.5 \times 10^7$ cm/s and a cascade fraction F = 0.45.

Table 4.2: Characteristic velocities (A/a) of scattered and recoil ions passing out through an amorphous silicon surface. It is important to note that in determining the characteristic velocities, the data with incident angles less than 8°, and exit angles less than 20° was ignored so as to reduce the effects of shadowing and blocking, and of surface roughness.

	Experiment (10^7 cm/s)	Ionization Potential (eV)	Scaled to square root of ionization potential (10^7 cm/s)
O^{2+}	5.5 ± 0.7	35.1	6.4
O^{+}	4.0 ± 0.4	13.6	(4.0)
Si^{3+}	2.4 ± 0.4	33.5	2.6
Si^{2+}	1.8 ± 0.2	16.3	(1.8)
Si^{+}	2.5 ± 0.3	8.1	1.3

correction important. For all the other ions the higher charge state has a yield which is an order of magnitude smaller, so that cascading was ignored in determining the characteristic velocities shown in Table 4.2.

Van der Weg and Bierman[20] have given the general relation for the sequential decay of many charge states. For the cascade decay of two states the rates of change of each population is defined by

$$\frac{dP_2}{dt} = -P_2 R_2(s)$$

and

$$\frac{dP_1}{dt} = +P_2 R_2(s) - P_1 R_1(s).$$

Again the Hagstrum type decay rate is assumed and these equations can be solved and integrated from the close encounter to $t = \infty$, with the result

$$P_2 = N \exp\left(-\frac{A_2}{av}\right)$$

and

$$P_1 = N \frac{A_2}{A_2 - A_1}\left[\exp\left(-\frac{A_1}{av}\right) - \exp\left(-\frac{A_2}{av}\right)\right].$$

If only a fraction F of the Si^{+} ions is produced at the close encounter, so that the remaining fraction $(1 - F)$ is the result of Si^{2+} decay as illustrated in Fig.4.8, then the Si^{+} yield becomes

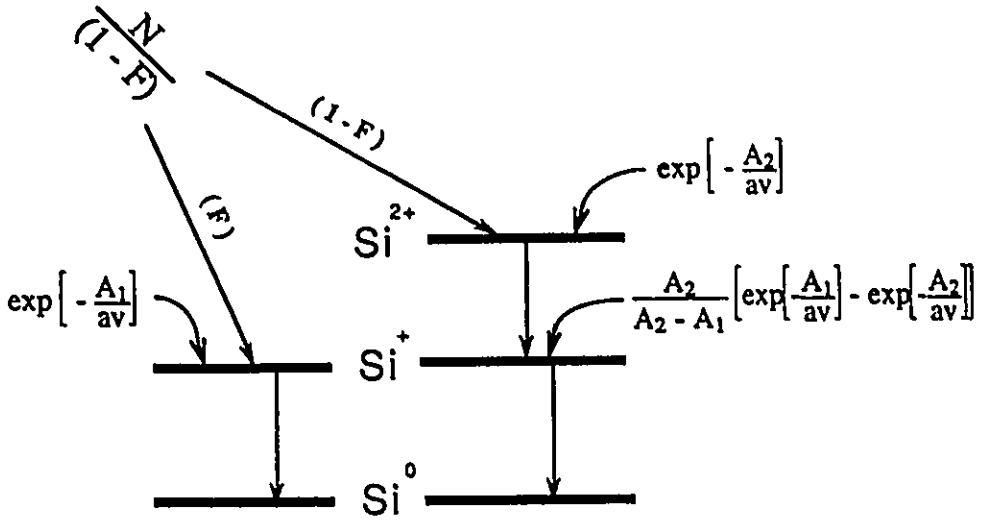

Figure 4.8: A close encounter can produce a Si^+ recoil ion, with fractional probability F, or a Si^{2+} ion with fractional probablity $(1 - F)$ which decays to Si^+ on the way out through the surface. The decay of the much fewer Si^{3+} ions and the reionization of neutral Si atoms which originate at the close encounter have been neglected.

$$P_1 = N\frac{A_2}{A_2 - A_1}\left[\left(1 + \frac{F(A_2 - A_1)}{(1-F)A_2}\right)\exp\left(-\frac{A_1}{av}\right) - \exp\left(-\frac{A_2}{av}\right)\right].$$

A value of 1.8×10^7 cm/s for A_2/a and the normalization N were obtained from the exponential fit to the Si^{2+} data. These values were then used in the fit to the Si^+ data. From the search for a fit it was found that a significantly higher characteristic velocity was required for Si^+ than for Si^{2+}. The fit was quite sensitive to the A_1 values, since $(A_1 - A_2)$ occurs in the denominator. In contrast the fit was not very sensitive to the value of F, and values in the range from $F = 0.3$ to $F = 0.6$ were acceptable, with the best fit at about $F = 0.45$.

It is interesting to compare the ratio of yields of the Si^+ to the Si^{2+} ions with the prediction of the cascade theory

$$\frac{P_1}{P_2} = \frac{A_2}{A_1 - A_2} - \frac{A_2 - A_1F}{(1-F)(A_1 - A_2)}\exp\left(-\frac{A_1 - A_2}{av}\right).$$

This relation is compared to experiment in Fig.4.7d) using the constants obtained from the fits of Fig.4.7b) and Fig.4.7c). The measurements of these ions were made simultaneously, so that they were obtained for the same number of incident ions, and exactly the same surface condition of the target. At small inverse velocities the rise in the ratio Si^+ to Si^{2+} can be associated with those Si^+ ions which originate at the close encounter and which decay faster than the Si^{2+} ions because of their larger characteristic velocity. Few of these ions must survive to our largest inverse velocities because the ratio reaches a nearly constant value corresponding to the dynamical equilibrium when the Si^{2+} and the Si^+ cascade decay rates become equal and the yields are in the ratio $A_2/(A_1 - A_2)$. It is remarkable that the experimental ratio of the charge yield gives a good fit to the theory out to large inverse velocities where each of the individual yields shown in Fig.4.7b) and Fig.4.7c) is several times the theoretical value. This is support for the assumption that the ion trajectories are charge independent. If there were significant differences, then surface roughness effects would not act equally on the Si^+ and the Si^{2+} ions, and there would not be such good cancellation in the ratio.

It is important to note that in all the plots there appear to be two approximately exponential decays. We interpret the variation at large $(v_o \, sin\phi_{out})^{-1}$, corresponding to small ϕ_{out} values and long interaction times, as an artifact due to departures from an ideally flat surface, and not to time dependence of the ion decay. Roughness of the surface can be expected to cause deviations from the calculated exit path length in two ways. On a macroscopic scale changes in the plane of the surface effectively change the local value of ϕ_{out}. On a microscopic scale, if atoms are missing from or added to the ideal surface, then there may be fewer or more atoms to interact with during its outgoing trajectory than calculated for an ideal surface.

The slopes at our lowest measured ϕ_{out}, in the range 5° to 10°, are approximately the same in all the five graphs of Fig.4.6 and Fig.4.7, suggesting that they are a characteristic of the surface and not of the ion. At the other extreme, where the entrance angles are small, shadow cone effects decrease the number of close encounters and hence the ion yield, so the data at these angles must also be ignored to obtain the characteristic velocity. This leaves the range of values of ϕ_{out} between

20° and 32° as the best region to use to determine the characteristic velocities. Here the data fit well to an exponential dependence, and both shadowing and surface roughness should be less intense.

4.3.1 Comparison with other measurements of characteristic velocities

Several characteristic velocities for ion surface decay of ion charges passing through surfaces have been previously reported. Nearly all are for rare gas ions on metal surfaces. Barth, Mühling and Eckstein[21] used 9 keV ion beams and found values between 1.9 and 3.4 $\times$ 10^7 cm/s for Ti^{2+} recoils, and 0.5 to 1.5 $\times$ 10^7 cm/s for Ti^+ recoils, with Ar^+ ions producing higher values than Ne^+ ions. Hsu and Rabalais[41] obtained 1.5 $\times$ 10^7 cm/s for Ne^+ scattering in the (100) plane from the surface layer atoms of Ni(001), and 0.6 $\times$ 10^7 cm/s for scattering in the (210) plane. The values found by Van der Weg and Bierman[20] at 60 keV and 90 keV for ion Ar^+ - Cu recoils are considerably smaller, 0.94 and 1.16 $\times$ 10^6 cm/s.

Verhey *et al.*[45] made detailed measurements of He^+-Cu(100) neutralization. They found that the value increased from 1.8 $\times$ 10^7 cm/s to 2.2 $\times$ 10^7 cm/s between 4 and 10 keV. Though they associated the ion decay with the outgoing interaction they found evidence for failure of the "loss of memory" assumption, since the exponential type interaction model only fitted the data with neutral incident beams, and not with incident ion beams. Their values are in excellent agreement with later measurements by Luitjens *et al*[19] with values of 1.65 $\times$ 10^7 cm/s at 5 keV and 2.24 $\times$ 10^7 at 10 keV. They also reported 1.5 $\times$ 10^7 cm/s for Ar^+ ions, and 1.0 $\times$ 10^7 cm/s for Ne^+ ions at 10 keV. There was some dependence on the orientation of the scattering plane with respect to crystallographic directions which could be associated with the proximity of the outgoing trajectory to a nearby atom.

The recent detailed fit by Eeken *et al.*[46] to the energy spectrum of the Auger electrons from Ar^{2+}-Pb collisions predicted that it is the Auger capture process which dominates the ion charge changing at the interaction distances which are relevant to our data, and the interaction has a strength which corresponds to a characteristic velocity of 2.3 $\times$ 10^7 cm/s for Ar^{2+} ions passing through the Pb(111)

surface on the way in.

Characteristic velocities have been reported where the variation of the perpendicular component of the outgoing velocity was obtained by changing the beam energy rather than the target angle[43]. However these data were obtained for varying distances of closest approach, and thus varying multicharged ion production at the close encounter, so they are not directly comparable to other characteritic velocities. From these existing data it is difficult to establish any systematic dependence of the characteristic velocities on properties of the beam and target. However in all cases where two charge states of the same ion on the same target have been measured, the higher charge state is found to have the higher characteristic velocity. Our observation that Si^{2+} has a lower characteristic velocity than the singly charged ion of the same element seems to be unique.

There is some theoretical justification for expecting that the transition rates would depend on the ionization potential of the transferred electron, which always increases with the ion charge state. The best result which Van der Weg and Bierman[20] found in their simultaneous fit of three charge states was obtained by assuming that the transition probabilites and therefore the characteristic velocities varied linearly with the ionization potentials. The detailed fit of Eeken *et al.*[46] was obtained assuming that the transition probabilities were linearly proportional to asymptotic tails of the wave functions, which for bound states have exponents which vary approximately as the square root of the binding energy of the electron. Their characteristic velocities were thus assumed to vary as the square root of the ionization potentials. For comparison the ionization potentials are given in Table 4.2, corresponding to the electron which is captured by the ion. The linear dependence assumed by Van der Weg and Bierman predicts too rapid a variation, and the last column shows the characteristic velocities scaled to a square root of these ionization potentials. Clearly the Si^{+} characteristic velocity cannot fit such dependence, but Si^{2+} and Si^{3+} are in agreement, and the O^{2+} to O^{+} ratio seems to be reasonably close.

There seems to be no common fit between different beam-target combinations. The oxygen characteristic velocities are twice those of Si for comparable ionization

potentials. In previously published data there is agreement that the rare gas characteristic velocities are not in the order of the ionization potentials with Ne^+ having the lowest values though it has an intermediate ionization potential between Ar^+ and He^+. It may be that the ionization potentials which are derived from ground state binding energies are not relevant to characteristic velocities because they are probably formed in excited states at the close encounter, which have quite different ionization potentials and different asymptotic wave function dependence than the ground state.

4.4 Multicharged ion yield dependence of Z_1 ($Z_1 < Z_2$)

There are large differences in the ion yields between $Z_1 = 6$ and $Z_1 = 10$. With the carbon beam, the yields from the surface consist almost completely of recoiling silicon ions, whereas with the neon beam we could detect only a small number of recoil ions, but there was a large yield of scattered ions. The differences cannot be associated with the ionization potentials, which increase from 11.2 eV in carbon to 21.5 eV in neon, so that loss of scattered ions to neutralization should be largest for the Ne^+ beam[47].

Not only are there more singly scattered ions with this beam, but relative to these there are more multiply scattered neon ions. The scattering cross section, in any of the forms which is used to fit ion-atom collisions increases continuously with Z_1, so that clearly some other interaction process than potential scattering is responsible for the opposite behaviour of the scattered and recoil ion yields. Fig.4.9 shows the relative yields of scattered (a) and recoil (b) ions which have made single atomic collisions as a function of the beam atomic number Z_1. For comparison these were all measured at the same collision velocity of 0.53 keV/amu. In calculating the yields, the areas under the peaks in the voltage scans were corrected for the variation of the ESA resolution with ion energy and with charge state.

As explained previously, a definite energy threshold was observed for the presence of multicharged ions. In all cases, as the beam energy was decreased, the ESA spectra simplified to only singly charged ion peaks and a continuous background from

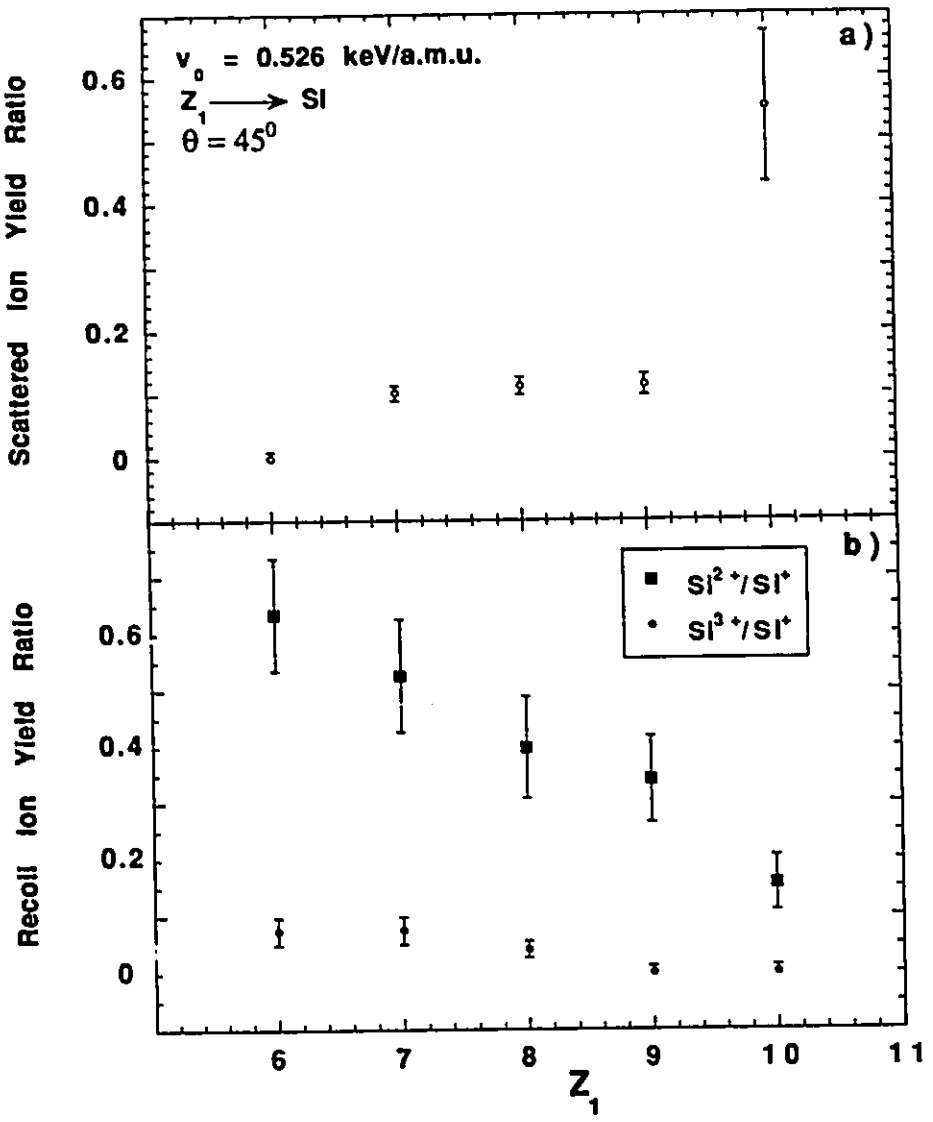

Figure 4.9: Relative yields of doubly and triply charged to singly charged ions, as a function of incident beam atomic number Z_1. Open circles are for (Doubly charged scattered ions)/(singly charged scattered ions). Open squares are for Si^{2+}/Si^{+}, and solid circles are for Si^{3+}/Si^{+}. (a) Scattered ions. (b) Recoil silicon ions.

subsurface scattering. The thresholds listed in Table 4.3 are the lowest beam energies at which the multicharged ion peak could be identified above the background. The existence of thresholds is consistent with interactions, which occur only at definite inter-atomic separations. The energy threshold for the multicharged ions can be compared with ion-gas collisions where there is a sudden increase in ionization of one, or both, of the scattered particles when the distance-of-closest-approach is small enough to reach a crossing of the molecular orbital correlation diagram at which inner shell vacancies can be produced[48]. Upon separation, these vacancies are filled mostly by Auger transitions.

We have made exact calculations of the ion-atom trajectories[6] using the "universal" potential which O'Connor and Biersack[1] found as the best fit to a wide range of scattering interactions. No adjustable parameters were used with this potential, but we found that it produced effectively identical shadow cone predictions to the Ziegler-Biersack-Lettmark potential[49] in which the screening length was used as an adjustable parameter so as to fit experimentally determined shadow cones[50]. Table 4.3 also lists the distances of closest approach (r_o), calculated using this potential at the measured threshold energies and scattering angles. These values are shown in Fig.4.10, where they are plotted as a function of the beam atomic number (Z_1).

Interpretation of electron vacancy production during ion–atom collisions is done in terms of the molecular orbital model. As the separation between the two particles decreases, the atomic electron states rearrange to fill molecular orbitals, subject to the Pauli principle. The relative energies of these states change with ion–atom separation, and electron transfer is thought to mainly occur when molecular orbital states mix at near-degeneracies. After the collision, the electrons may not return to their initial orbitals, and vacancies in lower energy orbitals are produced. A characteristic of the electron promotion model is that the near-degeneracy usually occurs at a definite particle separation which is called the crossing radius. If the trajectory does not bring the two particles close enough together to reach the crossing radius during the collision, then no vacancies are produced.

Table 4.3: Energy thresholds E_t, and distances-of-closest-approach r_o, calculated with the "universal" screened Coulomb potential of O'Connor and Biersack[1]. θ is the angle between the incident ion direction and the detected ion direction. θ' is the scattering angle when recoil Si ions are detected at θ. The error associated with each energy threshold value is $\Delta E = \pm 0.2$keV, as explained in Section 4.1.1. The errors on r_o were obtained by running the Molière scattering program at the two energy limits, $E+\Delta E$ and $E-\Delta E$, and finding the r_o at each limit.

Beam	θ	θ'	Doubly charged		Triply charged		Si^{2+}		Si^{3+}	
			E_t(keV)	$r_0(\AA)$	E_t(keV)	$r_0(\AA)$	E_t(keV)	$r_0(\AA)$	E_t(keV)	$r_0(\AA)$
C^+	40°	75°	12.5	0.128 ± 0.001			2.6	0.241 ± 0.009	3.1	0.221 ± 0.007
N^+	40°	72°	7.3	0.187 ± 0.003			3.8	0.217 ± 0.007	5.3	0.181 ± 0.004
O^+	40°	68°	5.8	0.228 ± 0.005	15.0	0.114 ± 0.002	5.5	0.195 ± 0.004	8.3	0.154 ± 0.002
F^+	40°	63°	3.8	0.300 ± 0.006	12.3	0.159 ± 0.002	7.4	0.181 ± 0.002	12.0	0.136 ± 0.002
Ne^+	50°	48°	0.8	0.558 ± 0.022	11.1	0.164 ± 0.002	9.8	0.179 ± 0.002	17.0	0.123 ± 0.001

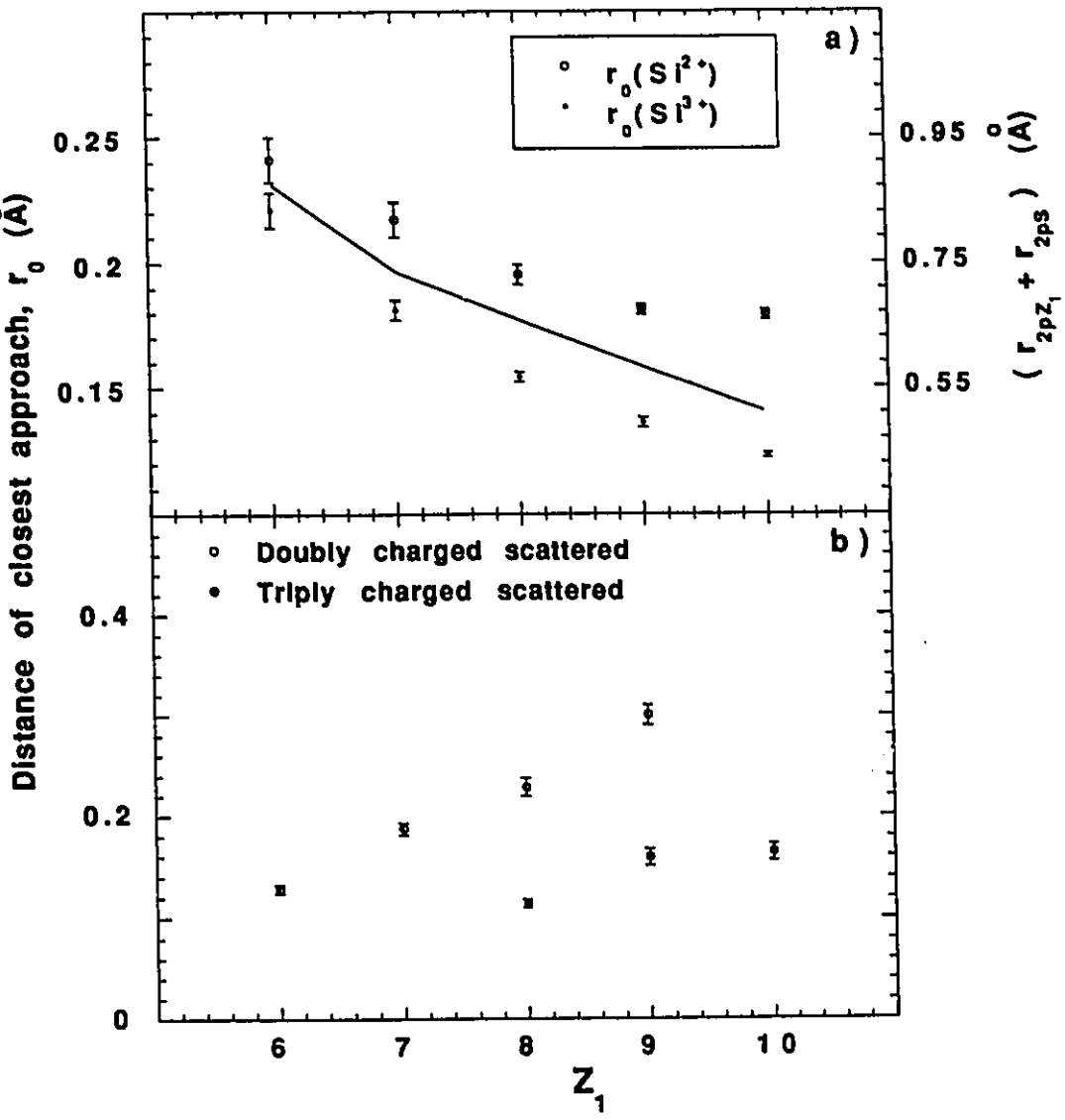

Figure 4.10: Distance of closest approach during single ion-atom collisions, calculated from the experimental energy thresholds and using a "universal" screened Coulomb potential[6]. Open circles are for doubly charged ions, and solid circles are for triply charged ions. (a) Silicon recoil ions; (b) Scattered incident ions. The line connects values of the sum of the atomic radii of the projectile and the target, calculated from the maximum of the Hartree-Fock electron densities[56].

The results obtained in this section can be compared with other information which is available on the Z_1 dependence of L-shell vacancy production. X-ray data show large oscillations in the target L-shell x-ray yields, both for solid targets[51], and for gases[52]. These oscillations reach their maximum value where there is a match between the target and projectile shell energies. The maxima are somewhat mismatched when the projectile x-rays in solid targets are measured, but the shift in position of the maximum is consistent with the level energy changes due to the projectile being in an excited or ionized state from previous collisions in the solid. Another characteristic of the x-ray data is that the x-rays from the lower Z atom are found to dominate on either side of the $Z_1 = Z_2$ maximum yield, so that target x-rays dominate where $Z_1 > Z_2$, and projectile x-rays where $Z_1 < Z_2$. The present data seem to fit the shell matching interpretation of the x-ray data.

The Ne^+-Si data are on the lower Z_1 side of the maximum yield where the shells match at $Z_1 = Z_2$. Multiple ionization of the projectile Ne dominates, in agreement with the model. In C^+–Si, the high yield of multiply charged recoiling target ions may be due to this projectile-target combination being on the high Z_1 side of another maximum, where the K-shell energy of the projectile matches the L-shell energy of the silicon target atoms. The shell energies suggest that the maximum x-ray yield and therefore also the maximum multicharged ion production would be expected with a beryllium beam.

4.4.1 Si^{2+} and Si^{3+} recoil ion yields and energy thresholds ($Z_1 < Z_2$)

The production of Si^{2+} and Si^{3+} recoil ions in surface collisions decreases continuously from C^+ to Ne^+, and is accompanied by a corresponding decrease in the crossing radius (Fig.4.10a). These interaction distances can be associated with a crossing radius at which one or two of the six $2p$ shell electrons from Si, which occupy the $3d\sigma$ orbital of the temporary molecule are transferred to the $3p\pi$ orbital, so that these electrons are promoted to the $3p$ shell of Si when the atoms separate[5]. Figure 4.11 shows correlations diagrams where the molecular states, at finite atomic separation, diabatically connect the separated-atom energy levels to

the combined-atom levels having the same quantum numbers and symmetries.

The rules for drawing these diagrams are given by Barat and Lichten[48]. The diagrams are shown for C–Si and Ne–Si in Fig.4.11 and it can be seen that although there are differences in the level spacing, the level order is almost the same, and the same $3d\sigma$ to $3p\pi$ crossing is therefore likely to be responsible for electron promotion with all projectiles between C^+ and Ne^+. A crude estimate of the crossing radius was obtained by scaling the crossing radius in Ne^+–Ar where the correlation diagram energies have been calculated[53]. These have a quite similar Z_1/Z_2 ratio to N^+–Si and O^+–Si, and the level ordering is the same. It was estimated that the interaction radius should scale as $(Z_1 Z_2)^{-1}$, so that the $0.112\,\AA$ value in Ne^+–Ar would become $0.206\,\AA$ in N^+–Si, and $0.180\AA$ in O^+–Si, in rough agreement with the distance of closest approach for the recoil ions.

If the same $3d\sigma$ - $3p\pi$ crossing is also responsible for Si^{2+} and Si^{3+} ion production in C^+–Si, F^+–Si and Ne^+–Si, then a decrease in r_o with Z_1 is expected as the inner shell electrons become more tightly bound by the higher nuclear charge. The $(Z_1 Z_2)^{-1}$ scaling factor cannot be used here to estimate the Z_1 dependence, since this scaling assumes a constant Z_1/Z_2 ratio. However Fastrup *et al.*[54] made energy loss measurements in ion–Ar-gas collisions using several ion beams, and compared their experimental r_o values, which are associated with the promotion of one electron from the $2p$ shell[55], with the sum of the target and projectile $2p$ shell atomic radii. Though their experimental r_o values were always smaller than this sum, they showed the same Z_1 dependence.

The sum of the $2p$ shell radii, as given by Hartree-Fock calculations for the maxima in the electron density[56], are shown as a line in Fig.4.10a). There is rough agreement in the variation with Z_1 for both Si^{2+} and Si^{3+}, confirming that the recoil ions in all these ion-Si collisions are probably the result of the same level crossing. The values are everywhere too large by a factor of about 3, showing that there is considerable overlap of the wave functions, which are far from being atomic orbitals at these small nuclear separations. However the variation with Z_1 should be roughly valid.

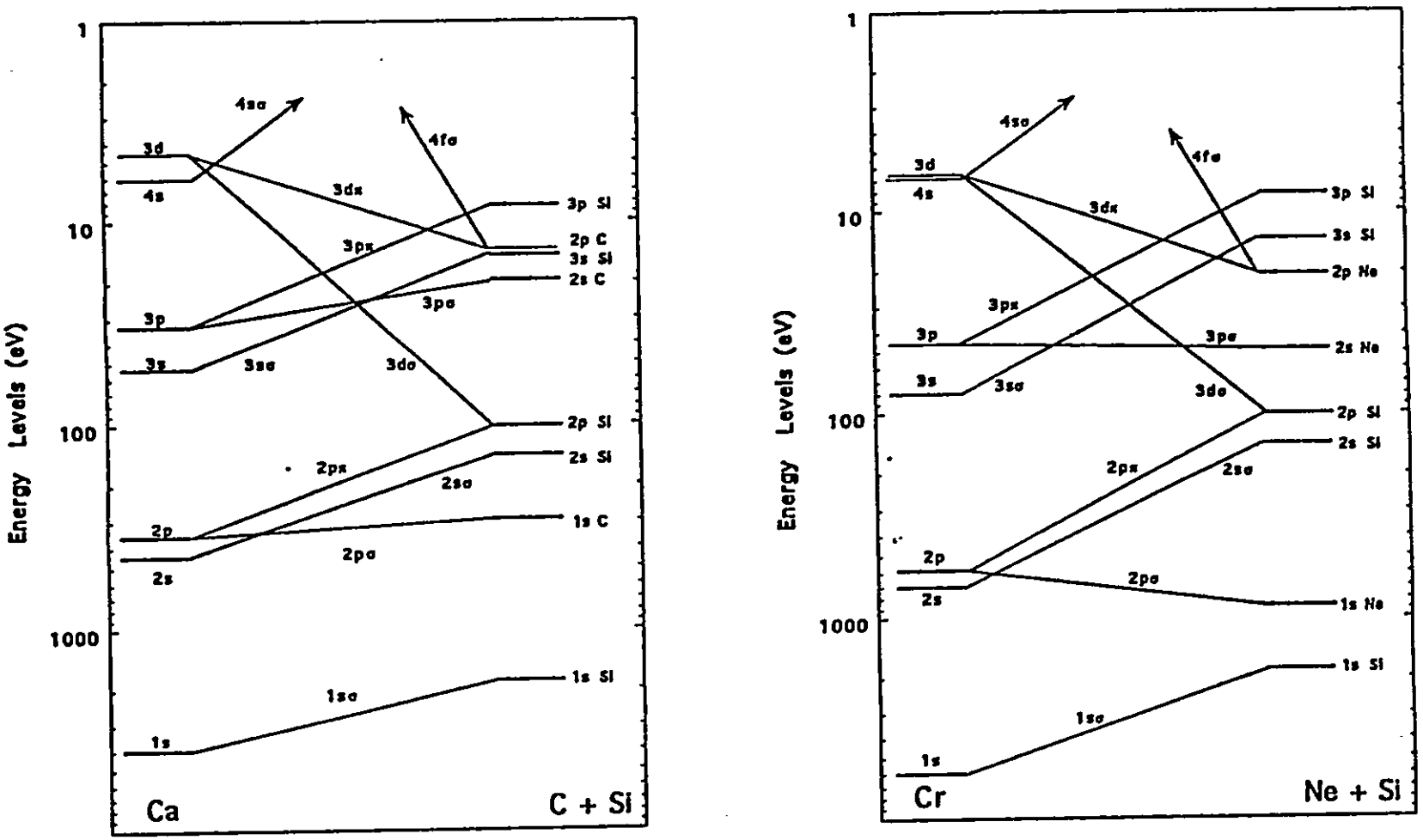

Figure 4.11: C–Si and Ne–Si correlation diagrams. The diabatic notation[48] is used to label the molecular orbitals which, in this approximation connect the atomic states at infinite separation to the united atom states.

The Si^{3+} crossing radii are always less than the corresponding Si^{2+} radii. A systematic difference is expected because of the increase in binding energy with the number of holes in the L-shell. Si^{3+} ions require more Auger transitions to further ionize the silicon recoil atom than do Si^{2+} ions, so it is likely that there is a correlation between the number of $2p$ shell holes which are produced in a collision, and the final recoil ion charge state which results. Larkins[57] has calculated the shell energies for Ar states having one or two L-shell vacancies. He found that the double hole states have binding energies about 15% greater than the equivalent single hole states. Such an increase in the binding energies could account for the observed decrease in the crossing radii.

4.4.2 Scattered multicharged ion yields and energy thresholds ($Z_1 < Z_2$)

The scattered ion yields have a strikingly different Z_1 dependence from the Si^{2+} and Si^{3+} recoil ion yields. We could detect no C^{3+} ions at all, and the C^{2+} yield was very small. The yield of multicharged scattered ions increases with Z_1, and is largest for Ne^{+} projectiles. The scattered ion yield correlates with the number of projectile $2p$ electrons, which increases from one electron in C^{+} to five in Ne^{+}. The $4f\sigma$ orbit is known to be important in electron promotion in many medium mass atomic collisions[58]. This orbital rises rapidly in energy, and crosses many other orbitals in the correlation diagram, so that electrons in this orbital can be promoted to higher shells, or be emitted. However, in contrast to recoil ions, the distance of closest approach at threshold energy, associated with the interaction distance r_o for production of these scattered ions is found to increase with Z_1. If $4f\sigma$ orbit promotion were the main source of projectile ionization then the interaction distances would be much larger than observed, and would decrease with increasing Z_1. The multicharged scattered ions must therefore be mainly from some other interaction process than simple $4f\sigma$ electron promotion.

A two electron transfer process has been found to be important in determining the final states following ion-gas single collisions. The two electrons make equal and opposite energy transitions in the same collision, so that though there is no crossing

in the correlation diagram for single electron state energies, the transition occurs at a near degeneracy in the correlation diagram for the total electron energy.

Energy loss spectroscopy measurements in ion - rare-gas collisions by Barat's group[59, 60] have identified in C^+–Ne and N^+–Ne the two electron transitions $(4f\sigma \rightarrow 3d\pi, 3d\sigma \rightarrow 3d\pi)$ as important in determining the final charge exchange channels. The interaction distances at which the two electron transitions take place depend on the relative spacings of the levels, which vary from one element to another. Applying the two electron transfer process to the present data, the $3s\sigma$ and $3d\pi$ levels change order between C^+ and Ne^+, so that if there is preferential ionization in the lower of the two states, then we would expect silicon ionization in C^+–Si collisions to change to neon ionization in Ne^+–Si collisions, as observed.

A difference between our data with the heavier silicon target and the ion – Ne-gas data, is that the $3d\sigma$ orbit is much lower in energy, so that the condition for equal and opposite energy transitions may be better satisfied at our observed distances of closest approach if the two electrons are transferred to the $3p\sigma$ orbital. The double electron transfer transitions $(4f\sigma \rightarrow 3s\sigma, 3d\sigma \rightarrow 3s\sigma)$ and $(4f\sigma \rightarrow 3d\pi, 3d\sigma \rightarrow 3d\pi)$, followed by Auger transitions to fill the $3d\sigma$ orbit may produce the multicharged scattered ions. $(4f\sigma \rightarrow 3d\pi, 3d\sigma \rightarrow 3d\pi)$ double electron transfer transitions may also be responsible for some of the silicon multicharged ion production.

4.4.3 Singly charged recoil and scattered ion yield dependence on Z_1 ($Z_1 < Z_2$)

The singly charged ion yields shown in Fig 4.12 have a similar Z_1 behaviour to the multicharged ions, with mainly target recoil ions in C^+–Si and projectile ions in Ne^+–Si, suggesting that most of the singly charged ions are produced by the same process as the multicharged ions. This is consistent with a scattering processes in which there is loss of memory of the incident beam charge state, and very little potential scattering during which the singly charged incident ion preserves its initial charge.

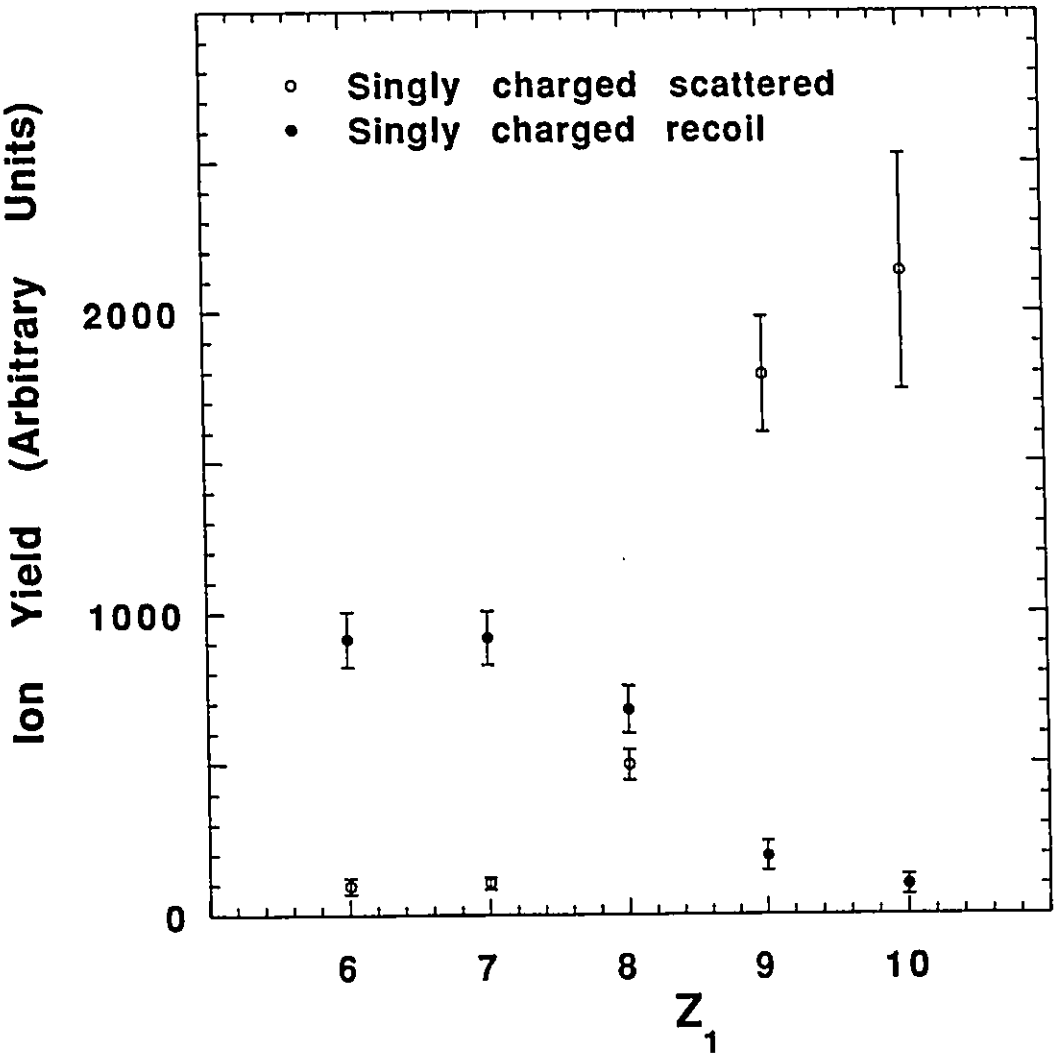

Figure 4.12: Yield of singly charged ions. Solid circles are for Si^+ recoil ions, and open circles are for scattered ions. There is some uncertainty in comparing the yields from different ion beams because of difficulties in normalization the beam intensities. This difficulty is not present when comparing the yields of different emitted ions from the same incident ion beam.

If the singly charged ions are the result of Auger transitions which fill L-shell vacancies, as are the multicharged ions, then it is rather surprising that we find no energy thresholds for the singly charged ions down to our lowest beam energies. The collision processes which produces these ions must therefore occur at a very large, or an indistinct interaction radius. Boers[4] reported memory effects in low energy Ne^+–Cu scattering, where he found different Ne^+/Ne ratios of scattered particles depending on the charge state of the incident beam. These differences decreased with increasing beam energy and were negligible at the energies used in Fig 4.9a). It may be possible to reconcile the lack of energy thresholds with the shell matching Z_1 dependence of the singly charged ion yields by assuming that there is a change in the interaction process, from mainly Auger deexcitation at energies of 10 keV and above, to mainly potential scattering at lower collision energies.

4.5 Multicharged ions dependence of Z_1 ($Z_1 > Z_2$)

The dominance among the multicharged ions of scattered ions over recoil ions, which was found for $Z_1 < Z_2$ collisions on a silicon surface, is seen to be reversed for $Z_1 > Z_2$ collisions. No scattered multicharged ions could be detected up to 30 keV, whereas there are strong yields of Si^{2+} and Si^{3+} ions. Another difference is that for $Z_1 < Z_2$ some recoil ions were always observed, even when scattered ions predominated. The change-over from mainly scattered to mainly recoil ions is consistent with the oscillatory Z_1 dependence found in the x-ray yields from a Cu target[51] and from an argon target[52] when bombarded with low energy ions. The similarity shows that this is a general property of the vacancy production process. A qualitative comparison between multicharged ion and x-ray yields may be complicated by the partial neutralization of these ions before they leave the surface. Figure 4.13 shows the oscillatory aspect of the ion yield with Z_1.

We associate the distance-of-closest-approach at threshold energy r_o with the interaction radius at which those electron vacancies are produced which lead to multicharged ions. The $(3d\sigma - 3p\pi)$ crossing was identified in the previous section as the electron promotion process responsible for the Si^{2+} and Si^{3+} ion production.

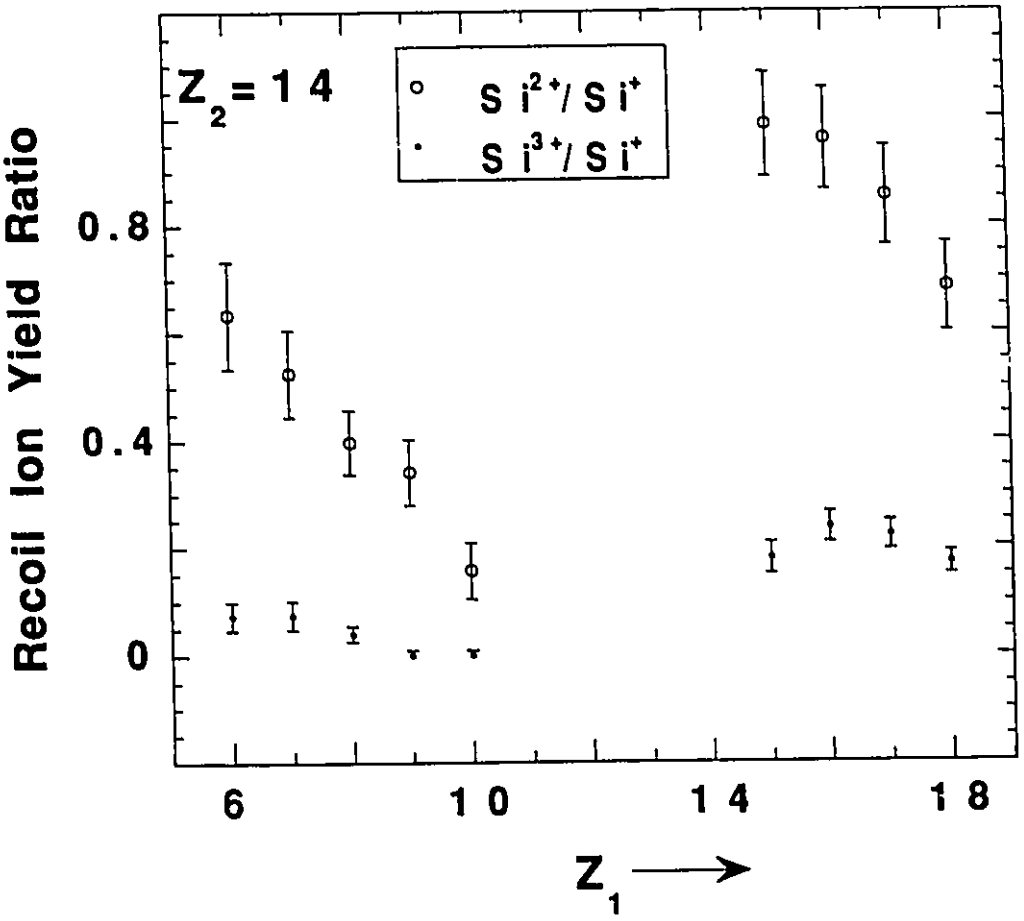

Figure 4.13: Yields of doubly and triply charged recoil ions as a ratio to the singly charged ions. Shown as a function of the atomic number of the incident beam (Z_1) and measured at the same beam velocity (0.53 keV/amu). Open circles are Si^{2+}/Si^{+}, solid circles are Si^{3+}/Si^{+}. Note that the data from the previous section (case where $Z_1 < Z_2$) is included.

Table 4.4: Threshold beam energies, and distances-of-closest-approach to create doubly and triply charged ions for a recoil angle of 38° with respect to the incident ions.

		Recoil Si^{2+}		Recoil Si^{3+}	
	θ'	E_{th} (keV)	$r_0(\AA)$	E_{th} (keV)	$r_0(\AA)$
$P^+ \rightarrow Si$	48.4°	1.0 ± 0.2	0.58 ± 0.004	2.6 ± 0.2	0.40 ± 0.02
$S^+ \rightarrow Si$	47.1°	1.5 ± 0.2	0.51 ± 0.03	2.9 ± 0.1	0.39 ± 0.02
$Cl^+ \rightarrow Si$	43.9°	2.2 ± 0.2	0.46 ± 0.02	4.0 ± 0.1	0.36 ± 0.01
$Ar^+ \rightarrow Si$	39.3°	4.0 ± 0.2	0.38 ± 0.01	5.1 ± 0.1	0.34 ± 0.01

The observed decrease in r_o with increasing Z_1, was consistent with the expected decrease in the crossing radius due to the increasing nuclear charge. These values of r_o are included for comparison in Fig.4.14. Calculations of the Ar – Si correlation diagram (Fig.2.6) predict a $(3d\sigma - 3p\pi)$ crossing radius of $0.10\AA$. Our r_o values are much larger than this, so that the recoiling multicharged ions in the present measurements are clearly not produced at the $(3d\sigma - 3p\pi)$ crossing.

The molecular orbital level ordering is such that the $(3d\sigma - 3p\pi)$ crossing promotes electrons in the atom with the higher Z_1 value, in agreement with the production of vacancies in the silicon target atoms for ion beams from C^+ to Ne^+. The $3p$ shell is not full in P^+, S^+, Cl^+ or Ar^+, so that the $(3d\sigma - 3p\pi)$ crossing is still available to promote $2p$ electrons, and this crossing could in principle result in the further ionization of each of these elements. However this seems not to be the case.

The Ar–Si correlation diagram[58] shows that the $4f\sigma$ orbital rises steeply and crosses many higher orbits at about $0.37\AA$. This is in rough agreement with the r_o value we find for the distances-of-closest-approach for Si^{2+} and Si^{3+} production (see Table 4.4). The orbital originates in the $2p$ electrons of the lighter of the two atoms in the collision, and so electron transfer from this orbital produce Si $2p$ shell vacancies after separation. The $4f\sigma$ orbital, and not the $3d\sigma$ orbital, can therefore be identified as the source of recoil atom vacancies, and hence of the multicharged recoil ions in these collisions.

It is possible to understand the smaller r_o values which were found for the Si^{3+} compared to those for the Si^{2+} production because at least one more vacancy in

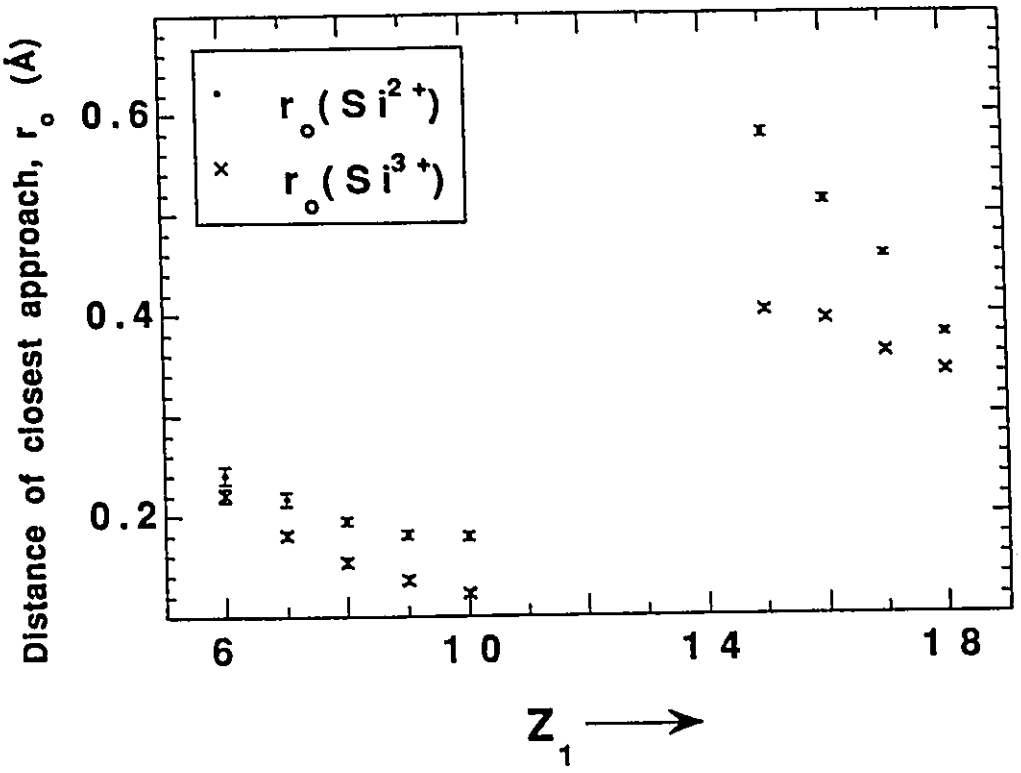

Figure 4.14: Distance of closest approach r_0 at the threshold energy as a function of Z_1. These values were obtained from exact calculations of the ion-atom trajectories which result in a 38° scattering angle at the threshold beam energy. The calculations assumed the "universal" screened Coulomb potential of O'Connor and Biersack[1]. The values of r_o and the threshold energies are also shown in Table 4.4.

the $4f\sigma$ orbital is required for the extra Auger transitions. The orbital energy is depressed by the extra hole correlation energy, and the crossings therefore occur at smaller interaction distances.

Chapter 5. Conclusions

The standard $\pi/\sqrt{2}$ electrostatic analyser design was modified so that a) it could accept ions emitted from the target over a wide solid angle, and b) it was compact enough to be installed inside a small UHV chamber in order to energy analyze ions emitted from target surfaces. Our modifications to the original design increase the detection efficiency to the level where it is possible to obtain energy spectra with beam fluxes which do not significantly damage the surface structure, and at the same time it is possible to make angular distribution measurements over a wide range of scattering angles. Because of our use of an ESA, we were able to identify multiply charged ions which were created in surface collisions. This led to the first systematic explorations of such ion production and decay and preempted surface structure investigations for which the system was designed.

Multiply charged ions which are produced during ion-Si surface scattering are found to be relatively abundant in some cases. For example, in N^+- Si surface scattering we can obtain up to 15% of the scattered ions being emitted as N^{2+}, and up to 40% of the recoil ions as Si^{2+}, and up to 6% as Si^{3+} ions. There is no ambiguity in which of the three interaction regions the multicharged ions decay by partial neutralization as may occur for singly charged ions, since they are created at the close encounter.

The neutralization along the outgoing path seems to be described by the Hagstrum exponential model, at least over a limited range of trajectories, but it is difficult to distinguish the failure of the model from surface roughness effects. The characteristic velocities which parametrize this model do not seem to fit the ionization dependence which was assumed by Van der Weg and Bierman, and a square root dependence may be more appropriate. The increase in the transition rate when an ion passes near to an atom during the outgoing trajectory, which has been observed for singly charged ions scattered from single crystal surfaces, may contribute to the

observed departure from exponential decay. It is possible that the angular variation of the multicharged ion yields may provide a useful supplement to channelling and blocking data when using ion scattering as a technique to determine surface structure.

There is a definite beam energy threshold at which each of these multicharged ions appears, which supports the theory that they are produced at definite atomic separations during close binary collisions. The interaction process is electron promotion from an inner shell, and the resulting vacancies are then filled by Auger de-excitation. Molecular orbital calculations can be used to estimate the atomic separations at which the diabatic crossings of these orbitals transfer an inner shell electron to an unfilled shell.

The results obtained when $Z_1 > Z_2$ are quite different compared to those obtained when $Z_1 < Z_2$. The multicharged yields seem to follow the same systematics as the x-ray yields i.e. that the x-ray yields increase as $Z_1 = Z_2$ is approached, and that when $Z_1 \approx Z_2$ inner shell promotion occurs mainly in the lower Z atom[51, 52]. Our technique determines the interaction radius for the production of these multicharged ions, and we find that on either side of $Z_1 = Z_2$ different molecular orbitals seem to be responsible for those electron promotions which result in multicharged ions as the holes are filled.

Future charge exchange investigations should concentrate on expanding the present multicharged ion survey by bombarding different target surfaces, such as germanium or aluminum which are readily prepared, with the same variety of ion beams. Aluminum samples might prove rather interesting since the atomic number of aluminum is closely similar to that of silicon, but it is a metal rather than a semiconductor. It would therefore be possible to determine whether there are differences in the characteristic velocities (A/a) due to conduction electron densities. It might also prove worthwhile to scatter positive as well as negative ion beams from the same surfaces. By examining the ion emission yields and multicharged ion energy creation thresholds, many questions regarding the memory loss of different projectiles upon scattering from a surface could be resolved. Another study which might prove profitable would be to examine the dependence of characteristic velocities on a) the

ionisation potential of different projectile ions, b) the kinetic energy of the incident particles and c) electronic surface properties such as the work function of the surface, the valence band width and the density of states at the surface. Since a main advantage of our system is the versality of the accelerator, i.e. monoenergetic beams of both positive and negative ions of many different elements with a wide range of primary energies, future investigations should be chosen with this in mind.

References

[1] D. J. O'Connor and J. P. Biersack, Nucl. Instrum. Methods **B 15**, 14 (1986).

[2] E. Taglauer and W. Heiland, Appl. Phys. **9**, 261 (1976).

[3] H. D. Hagstrum, Phys. Rev. **96**, 325 (1954); H. D. Hagstrum, Phys. Rev. **96** 336 (1954); H. D. Hagstrum, Phys. Rev. **119**, 940 (1960); H. D. Hagstrum, Phys. Rev. **122**, 83 (1961); H. D. Hagstrum, Phys. Rev. **150**, 495 (1966).

[4] A. L. Boers, Nucl. Instrum. Methods **B4**, 98 (1984).

[5] B. Hird, P. Gauthier, J. Bulicz and R. A. Armstrong, Phys. Rev. Lett. **67**, 3575 (1991).

[6] B. Hird, Exact screened Coulomb potential scattering calculations (unpublished).

[7] R. P. N. Bronckers and A. G. J. Wit, Surf. Sci. **104**, 384.

[8] J. Los and J. J. C. Geerlings, Phys. Rep. **190**, 133 (1990); R. Brako and D. M. Newns, Rep. Prog. Phys. **52**, 655 (1989).

[9] E. P. Suurmeijer, A. L. Boers, Surf. Sci. **43**, 309 (1973).

[10] S. Datz and A. C. Snoek, Phys. Rev. **134**, A347 (1964).

[11] S. S. Schekter, J. Exp. Theo. Phys. (USSR) **7**, 750 (1937).

[12] R. J. Macdonald and D. J. O'Connor. Surf. Sci. **124**, 423 (1983); R. J. Macdonald, D. J. O'Connor and P. R. Higginbottom. Nucl. Instr. Methods Phys. Res. **B2**, 418 (1984).

[13] W. Bloss and D. Hone. Surf. Sci. **72**, 277 (1978).

[14] Y. Muda and T. Hanawa. Surf. Sci. **97**, 283 (1980).

[15] J. W. Gadzuk, Surf. Sci. **6**, 133 (1967); **6**, 159 (1967).

[16] P. W. Anderson, Phys.Rev. **124**, 41 (1961); R. Brako and D. M. Newns, Surf. Sci. **108**, 253 (1981); R. Brako and D. M. Newns, Rep. Prog. Phys. **52**, 655 (1989).

[17] J. N. M. van Wunnik, J. J. C. Geerlings, E. H. A. Granneman and J. Los, Surf. Sci. **131**, 17 (1983).

[18] R. Souda, M. Aono, C. Oshima, S. Otani and Y. Ishizawa, Surf. Sci. **150**, L59 (1985); T. M. Thomas, H. Neumann, A. W. Czandarna and J. R. Pitts, Surf. Sci. **175**, L737 (1986); R. M. McCune, J. E. Chelgren and M. A. Z. Wheeler, Surf. Sci. **84**, L515 (1979).

[19] S. B. Luitjens, A. J. Algra, E. P. Th. M. Suurmeijer and A. L. Boers, Surf. Sci. **99**, 631 (1980).

[20] W. F. Van der Weg and D. J. Bierman, Physica, **44**, 177 (1969).

[21] H. J. Barth, E. Mühling and W. Eckstein, Surf. Sci. **166**, 458 (1986).

[22] H. Winter, Nucl. Instrum. Methods **B2**, 286 (1984).

[23] J. D. Garcia, R. J. Fortner and T. M. Kavanagh, Rev. Mod. Phys. **45**, 111 (1973); M.E.Rudd and J.Macek, *Case Studies in Atomic Physics*, edited by M. R. C. McDowell and E. W. McDaniel (Amsterdam, North Holland, 1972), Vol. 3, p. 47; G. N. Ogurtsov, Rev. Mod. Phys. **44**, 1 (1972).

[24] G. Zampieri, F. Meier and R. Baragiola, Phys. Rev. **A29**, 116 (1984).

[25] S. T. deZwart, A. G. Drentje, A. L. Boers and R. Morgenstern, Surf. Sci. **217**, 298 (1989); P.Varga, *Electron and Atomic Collisions*, Edited by H. B. Gilbody, W. R. Newell, F. H. Read and A. C. H. Smith (Elsevier, Amsterdam, 1988), p.793.

[26] J. F. Hennequin, P. Joyes and R. Casting, Comp. Rend. **265B**, 315 (1967).

[27] J. Maul and K. Wittmaack, Surf. Sci. **47**, 358 (1975); K. Wittmaack, Nucl. Instrum. Methods, **170**, 565 (1980).

[28] R. A. Baragiola, L. Nair and T. E. Madey Nucl. Instrum. Methods, **B58**, 322 (1991).

[29] O. Grizzi and R. A. Baragiola, Phys. Rev. A**35**, 135 (1987).

[30] A. Oliva, A. Bonanno, M. Camarco and F. Xu, Nucl. Instrum. Methods, **B58**, 333 (1991).

[31] M. H. Shapiro and J. Fine, Nucl. Instrum. Methods, **B44**, 43 (1989).

[32] S. Valeri, Surf. Sci. Reports, **17**, 85 (1993).

[33] H. D. Betz and L. Grodzins, Phys. Rev. Lett. **25**, 211 (1970).

[34] J. R. Pierce, *Theory and Design of Electron Beams*, (Van Nostrand, 2nd Ed. 1954), Chapter IX.

[35] H. Bu, M. Shi and J. W. Rabalais, Surf. Sci. **224**, 96 (1991).

[36] C. D. Roux, H. Bu and J. W. Rabalais, Surf. Sci **279**, 1 (1992).

[37] O. Grizzi, M. Shi and J. W. Rabalais, Rev. Sci. Instrum. **61**, 740 (1990).

[38] A. L. Hughes and V. Rojansky, Phys. Rev. **34**, 284 (1929).

[39] K. Komaki and F. Fujimoto, Jpn. J. Appl. Phys. **21**, L521 (1982).

[40] J. S. Williams, M. C. Ridgway, R. G. Elliman, J. A. Davies, S. .T. Johnson and G. R. Palmer, Nucl. Instr. Methods, B **55**, 602 (1991).

[41] C. C. Hsu and J. W. Rabalais, Surf. Sci. **256**, (1991) 77.

[42] R. E. Schlier and H. E. Farnsworth, J. Chem. Phys. **30**, 917 (1959).

[43] J. W. Rabalais, J-N. Chen, R. Kumar and N. Narayana, J. Chem. Phys. **83**, 6489 (1985).

[44] J-N. Chen, M. Shi, S. Tachi and J. W. Rabalais, Nucl. Instrum. Methods **B 16**, 91 (1986); J. Fricke, A. Müller and E. Salzborn, Nucl. Instrum. Methods **175**, 379 (1980).

[45] L. K. Verhey, B. Poelsema and A. L. Boers, Nucl. Instr. Methods **132**, 565 (1976).

[46] P. Eeken, J. M. Fluit, A. Niehaus and I. Urzgil'din, Surf. Sci. **273** (1992) 160.

[47] G. Verbist, J. T. Devreesse and H. H. Brongersma, Surf. Science **233**, 323 (1990).

[48] M. Barat and W. Lichten, Phys. Rev. **A6**, 211 (1972).

[49] J. F. Ziegler, J. P. Biersack and V. Littmark in *The Stopping and Range of Ions in Solids* (Permagon, New York, 1985).

[50] H. Bu, M. Shi and R. W. Rabalais, Nucl. Instrum. Methods B **61**, 337 (1991).

[51] T. M. Kavanagh, M. E. Cunningham, R. C. Der, R. J. Fortner, J. M. Khan, and E. J. Zaharis, Phys. Rev. Lett. **25** 1473 (1970).

[52] F. W. Saris and D. J. Bierman, Phys. Lett. **35A**, 199 (1971).

[53] F. P. Larkins, J. Phys. **B5**, 571 (1972).

[54] B. Fastrup, G. Hermann and K. J. Smith, Phys. Rev. **A3**, 1591 (1971).

[55] U. Fano and W. Lichten, Phys. Rev. Lett. **14**, 627 (1965).

[56] J. P. Desclaux, Atomic Data and Nuclear Data Tables **12**, 311 (1973).

[57] F. P. Larkins, J. Phys.**B4**, 1 (1971).

[58] D. Schneider, G. Nolte, U. Wille, and N. Stolterfoht, Phys. Rev. **A28**, 161 (1983).

[59] D. Dowek, J. Krutein, U. Thielmann, J. Fayeton, and M. Barat, J. Phys. **B12**, 2553 (1979).

[60] U. Thielmann, J. Krutein, and M. Barat, J. Phys.**B13**, 1217 (1980).